Oligomerization of a molecular chaperone modulates its activity

Tomohide Saio[1,2,3*], Soichiro Kawagoe[2], Koichiro Ishimori[1,2] & Charalampos G. Kalodimos[4*]

[1]*Department of Chemistry, Faculty of Science, Hokkaido University, Sapporo 060-0810, Japan*

[2]*Graduate School of Chemical Sciences and Engineering, Hokkaido University, Sapporo 060-0810, Japan*

[3]*PRESTO, JST*

[4]*Department of Structural Biology, St. Jude Children's Research Hospital, Memphis, TN 38105, USA*

* Corresponding authors. E-mail: saio@sci.hokudai.ac.jp, babis.kalodimos@stjude.org

Abstract

Molecular chaperones alter the folding properties of cellular proteins via mechanisms that are not well understood. Here we show that Trigger Factor (TF), an ATP-independent chaperone, exerts strikingly contrasting effects on the folding of non-native proteins as it transitions between a monomeric and a dimeric state. We used NMR spectroscopy to determine the atomic resolution structure of the 100-kDa dimeric TF. The structural data show that some of the substrate-binding sites are buried in the dimeric interface, explaining the lower affinity for protein substrates of the dimeric compared to the monomeric TF. Surprisingly, the dimeric TF associates faster with proteins and it exhibits stronger anti-aggregation and holdase activity than the monomeric TF. The structural data show that the dimer assembles in a way that substrate-binding sites in the two subunits form a large contiguous surface inside a cavity, thus accounting for the observed accelerated association with unfolded proteins. Our results demonstrate how the activity of a chaperone can be modulated to provide distinct functional outcomes in the cell.

Introduction

Molecular chaperones typically prevent the aggregation and assist with the folding of non-native proteins (Balchin et al., 2016; Bukau et al., 2006). Thus, chaperones are central to protein homeostasis in the cell and are essential for life (Hipp et al., 2014; Powers and Balch, 2013). Recent studies have also highlighted molecular chaperones as inhibitors of amyloid formation (Mainz et al., 2015; Taylor et al., 2016). Despite major advances in the field, how chaperones engage and alter the folding properties of non-native proteins remain poorly understood (He et al., 2016; Huang et al., 2016; Koldewey et al., 2016; Libich et al., 2015; Rosenzweig et al., 2017; Saio et al., 2014; Sekhar et al., 2016; Verba et al., 2016; Walti et al., 2017). Despite common features, the mechanisms of activity are distinct in different families of chaperones (Mattoo and Goloubinoff, 2014). Studies of ATP-dependent chaperones, such as the Hsp70 and GroEL systems, have shown how cycles of ATP binding, hydrolysis and nucleotide release can give rise to different conformational states that exhibit distinct affinities for the substrate protein (Apetri and Horwich, 2008; Clare et al., 2012; Hayer-Hartl et al., 2016; Kampinga and Craig, 2010; Mayer and Bukau, 2005; Saibil et al., 2013; Sekhar et al., 2016; Zhuravleva et al., 2012). Much less is known about how ATP-independent chaperones assist with protein folding (Stull et al., 2016).

The Trigger Factor (TF) chaperone has several unique features (Hoffmann et al., 2010; Ries et al., 2017; Wruck et al., 2017): (i) is the only ribosome-associated chaperone in bacteria; (ii) with an estimated cellular concentration of ~50 μM (Crooke et al., 1988) it is also the most abundant one; (iii) in contrast to other oligomeric chaperones such as GroEL, SecB, and Hsp90 that form stable oligomers, TF undergoes a dynamic transition between a monomeric and a dimeric form; (iv) TF functions both at the ribosome and in the cytosol: it

52 binds, as a monomer, next to the exit channel at the ribosome to prevent the aggregation and
53 premature folding of nascent polypeptides, while it functions as a dimer in the cytosol where
54 is thought to assist in various processes in protein folding and biogenesis (Agashe et al.,
55 2004; Ferbitz et al., 2004; Haldar et al., 2017; Martinez-Hackert and Hendrickson, 2009; Oh
56 et al., 2011; Ullers et al., 2007). TF is also being widely used as a co-expression factor to
57 improve the folding and yield of soluble proteins in biotechnology (Uthailak et al., 2017).
58 We recently determined the atomic resolution structure of TF in complex with a non-
59 native protein (Saio et al., 2014). The structure revealed how the chaperone recognizes and
60 engages the non-native protein and how it retains it in an unfolded state. Interestingly, our
61 data showed that substrate protein binding causes TF to monomerize, thus indicating that
62 the substrate-binding sites are occluded in dimeric TF. The interplay between substrate
63 protein binding and chaperone oligomerization is likely to be used as a mechanism to
64 modulate the energetics and kinetics of interaction in chaperone-substrate protein
65 complexes, as for example in small heat shock proteins (Eyles and Gierasch, 2010). The large
66 size of the dimeric TF (100 kDa) and its apparent dynamic nature has hindered
67 determination of its structure.
68 We have taken advantage of recent advances in NMR spectroscopy and isotope
69 labeling (Huang and Kalodimos, 2017) to determine the atomic structure of dimeric TF. The
70 structure shows that three out of the five substrate-binding sites are partially buried in the
71 dimer, thus explaining why protein binding results in TF monomerization. Interestingly, the
72 dimer assembles in such a way that substrate-binding sites in the two subunits form a large
73 contiguous surface inside a cavity. The structural data explain the unexpected finding that
74 non-native proteins appear to bind with higher association rate to the dimeric TF than to the

75 monomeric TF. Activity assays showed that TF dimerization enables the chaperone to exhibit
76 stronger holdase and anti-aggregation activity.
77

78 Results

79 Characterization of TF dimerization. *Escherichia coli* TF consists of 432 amino acids,
80 comprising RBD (residues 1 to 112), PPD (residues 150 to 246), and SBD (residues 113 to

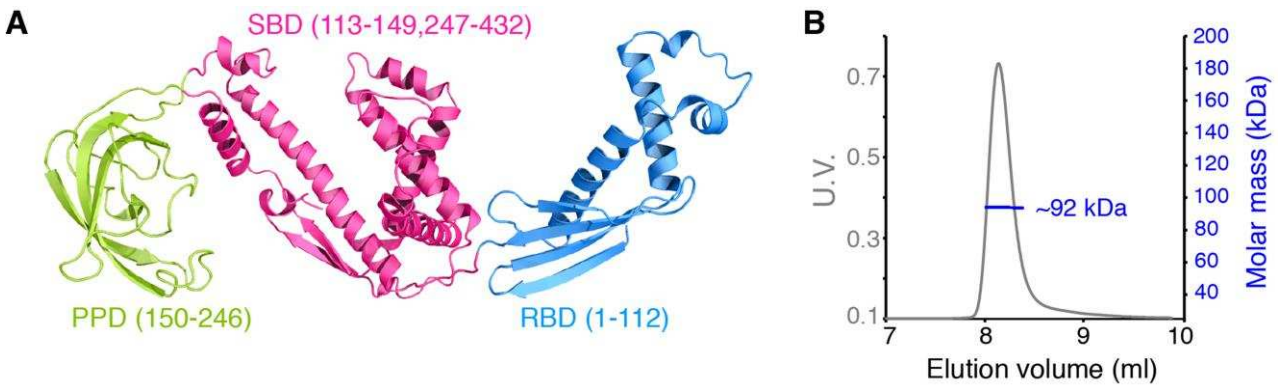

Figure 1. Dimerization of TF in solution. (*A*) Structure of *E. coli* TF (PDB code: 1W26). PPD, SBD, and RBD are shown in green, pink, and blue, respectively. The residue boundaries for each one of the three domains are shown in parentheses. SBD is discontinuous and is formed primarily by the C-terminal domain. (*B*) Size exclusion chromatography (SEC)-MALS of unliganded TF shows that the protein forms a dimer (Theoretical molar mass: 96 kDa) in solution.

81 149 and 247 to 432) (Figure 1*A*). Both multi-angle light scattering (MALS) and NMR studies
82 show that TF forms a dimer of ~100 kDa in solution (Figure 1*B* and **Figure 1-figure**
83 **supplement 1*A***). MALS and analytical ultracentrifugation (AUC) experiments yielded a
84 dimerization dissociation constant (K_d) of ~2 μM (**Figure 1-figure supplement 1 *B-D***), which
85 is similar to previously reported values (Kaiser et al., 2006; Maier et al., 2003; Morgado et al.,
86 2017). TF monomerization induced by substrate binding was previously reported (Saio et

al., 2014) and has been further corroborated in the present work by MALS and NMR (**Figure 1-figure supplement 1** ***A, E,*** **and** ***F***). The intrinsic dissociation rate (k_{diss}) of the dimer was measured by tryptophan fluorescence following rapid dilution of TF (**Figure 1-figure supplement 1*G***). Fitting of the data to a single exponential function resulted in k_{diss} of ~10 s^{-1}, which indicates that the dimer is quite dynamic and thus the exchange between formation and dissociation of the dimer can be a major cause of the line broadening observed for the resonances located in RBD (Morgado et al., 2017) (Saio et al., 2014). This is further supported by the observation that line broadening at the interface of dimeric TF is suppressed in concentrated TF samples (~1 mM; Fig. S2). Previous studies employing fluorescent labeling (Kaiser et al., 2006) or (1-oxyl-2,2,5,5-tetramethyl-3-pyrroline-3-methyl)-ethanethiosulfonate (MTSL) spin labeling tags (Morgado et al., 2017) reported slower dissociation rates, likely due to the strong hydrophobic nature of the tag.

Structure of dimeric TF. We used NMR spectroscopy to determine the structure of the 100 kDa dimeric form of TF in solution (see Materials and methods). We used U-^{12}C,^{15}N-labelled TF samples that contained specifically protonated methyl groups of Ala, Val, Leu, Met, Thr and Ile (δ1) and protonated aromatic residues Phe, and Tyr in an otherwise deuterated background (Huang and Kalodimos, 2017; Tzeng et al., 2012) (**Figure 2-figure supplement 1**). The high sensitivity and resolution of the methyl region, combined with the high abundance of these eight amino acids in TF (**Figure 2-figure supplement 1**) and in the dimeric TF interface provided a large number of intra- and inter-molecular nuclear Overhauser effects (NOEs) (**Table 1**).

Table 1. Structural and NMR statistics of TF dimer.

Distance restraints[a]	
NOEs	
Short range (intraresidue and sequential)	870
Medium range ($2 \leq \mid i\text{-}j \mid \leq 5$)	467
Long range ($\mid i\text{-}j \mid > 5$)	1230
Intermolecular	54
Hydrogen bonds	374
Dihedral angle restraints (φ and ψ)	1358
Violations (mean and SD)[a]	
Distance restraints (Å)	0.005 ± 0.025
Dihedral angle restraints (°)	0.02 ± 0.23
Structural coordinates rmsd[a]	
RBD core (1-39, 51-112)	
Chain A	
Backbone atoms	1.50 ± 0. Å
All heavy atoms	2.04 ± 0.29 Å
Chain B	
Backbone atoms	1.56 ± 0.41 Å
All heavy atoms	2.07 ± 0.38 Å
PPD core (157-190,195-241)	
Chain A	
Backbone atoms	0.87 ± 0.09 Å
All heavy atoms	1.38 ± 0.07 Å
Chain B	
Backbone atoms	0.82 ± 0.14 Å
All heavy atoms	1.30 ± 0.11 Å
SBD core (115-149, 250-321, 329-428)	
Chain A	
Backbone atoms	1.40 ± 0.21Å
All heavy atoms	2.17 ± 0.23 Å
Chain B	
Backbone atoms	1.34 ± 0.16Å
All heavy atoms	2.14 ± 0.20 Å
Ramachandran plot[a]	
Most-favored regions	85.4%
Additionally allowed regions	14.3%
Generously allowed regions	0.3%
Disallowed regions	0.0%

[a]The statistics apply to the 20 lowest-energy structures.

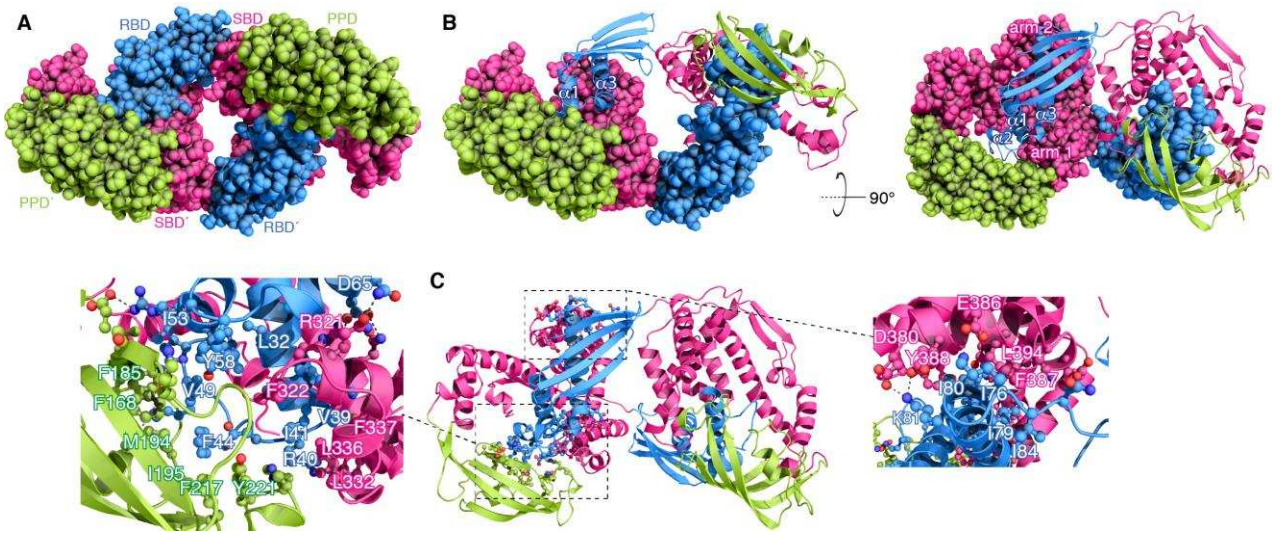

Figure 2. Structural basis for TF dimerization. (*A*) The lowest-energy structure of the TF dimer is shown as space-filling model. TF forms a dimer in a head-to-tail orientation. RBD, SBD, and PPD are shown in blue, magenta, and green, respectively. (*B*) One of the TF subunits is shown as space-filling model and the other subunit shown in ribbon. The helices of the RBD and the two arm regions are labeled. (*C*) Expanded views of the dimeric interfaces highlighting contacts between the two subunits. Residues involved in mediating dimerization are shown as ball-and-stick.

The structure of dimeric TF is shown in Figure 2. TF forms a symmetric dimer in a head-to-tail orientation. Part of RBD inserts into a large cavity that is formed between the SBD and PPD of the other subunit (Figure 2 ***A*** and ***B***) and the arrangement results in three major interfaces that hold the dimer together (Figure 2***C***). The three helices in RBD (α1-α3) form extensive contacts with PPD and the SBD arm 1 and arm 2 regions. Specifically, a hydrophobic patch in SBD arm 1 consisting of bulky hydrophobic residues (Leu314, Phe322, Leu332, Leu336, and Phe337) forms intimate nonpolar contacts with the C-terminal region of RBD helix α1 (Val35, Ala36, Val39, and Ile41) (Figure 2***C***). This binding interface is further

strengthened by a salt bridge between Arg40 and Glu339 and a hydrogen bond between Lys38 and Gln340. SBD arm 1 also interacts with the N-terminal part of RBD helix α3 exclusively via polar contacts (e.g. between Asp65 and Arg321) (Figure 2*C*). 2,540 Å^2 (1,620 Å^2 nonpolar and 920 Å^2 polar) of surface are buried in this interface of the dimer. A large hydrophobic patch in PPD consisting of aromatic and bulky nonpolar residues (Phe168, Phe185, Met194, Ile195, Tyr221) engages the long loop in RBD connecting helices α1 and α3, which also features a short helix (α2). Residues Phe44, Val49, Ile53, and Tyr58 in RBD appear to establish the most important contacts with PPD, including two salt bridges (between Arg57 and Asp184 and between Lys48 and Glu199) (Figure 2*C*). 2,650 Å^2 (1,900 Å^2 nonpolar and 750 Å^2 polar) of surface are buried in this interface. The third major dimeric interface is mediated by SBD arm 2 and the C-terminal region of RBD helix α3. Similarly to the other two, this interface is made up primarily of nonpolar residues (RBD residues Ile76, Ile79, Ile80 and Ile84; SBD residues Val384, Tyr388, Phe387, and Leu394) with additional salt bridges at the periphery of the binding site. 1,480 Å^2 (1,050 Å^2 nonpolar and 430 Å^2 polar) are buried at this dimeric interface, which is the smallest among the three ones. A total surface of 6,670 Å^2 is buried upon dimer formation. The extensive interface seen in the structure to mediate the dimer was tested by mutagenesis and a triple amino-acid substitution variant (V39E/I76E/I80A; hereafter TF^{mon}) was identified that abolishes TF dimerization (**Figure 2-figure supplement 2**). A recently reported low-resolution structural model of TF dimer also showed a head-to-tail orientation of the two subunits (Morgado et al., 2017). However, the dimeric interface is very different from the one observed in our structure (**Figure 2-figure supplement 3**).

Superposition of the crystallographically determined structure of the monomeric TF (Ferbitz et al., 2004) on one of the subunits of the dimeric TF demonstrates that TF undergoes major conformational changes as it transitions from the monomeric to the dimeric state (**Figure 3*A***). With respect to SBD, RBD undergoes a 60° rotation and a 21 Å translation, whereas PPD undergoes a 74° rotation and a 19 Å translation. As a result, PPD moves closer to SBD within the same subunit, and the two domains form a large cavity wherein the RBD of the other subunit inserts into (**Figure 2** and 3***A***). These conformational changes results in a more compact TF structure in the dimeric form, which is consistent with small-angle X-ray scattering (SAXS) data (Ries et al., 2017).

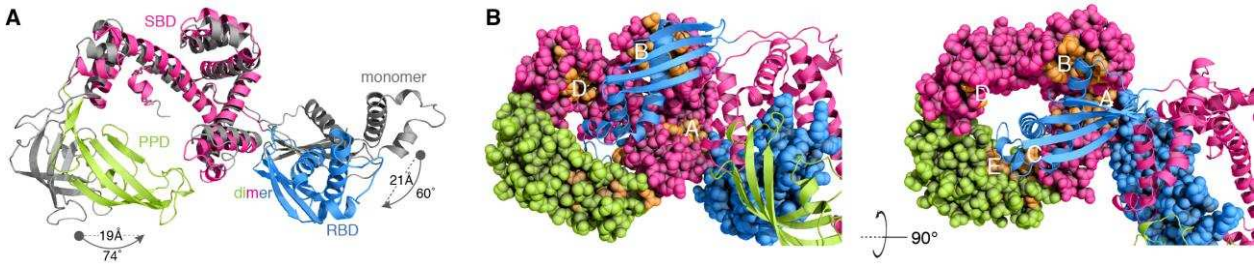

Figure 3. Conformational changes of TF upon dimerization. (*A*) The structure of one subunit in the TF dimer (colored as in Figure 1A) and the crystal structure of monomeric TF (colored grey) [Protein Data Bank (PDB) code: 1W26] are superimposed for SBD. The changes in rotation and translation of the RBD and PPD between the monomer and the dimer are indicated. (*B*) View of the structure of dimeric TF highlighting the positioning of the substrate-binding sites (colored orange). The five main substrate-binding sites are labeled A, B, C, D, and E.

Dimerization buries the ribosome- and substrate-binding sites. The structural data suggest that TF dimerization has profound impact on the function of TF because the ribosome-binding region as well as several of the substrate-binding sites are buried in the dimer (**Figure 3*B*** and **Figure 3-figure supplement 1**). The RBD loop, which contains the signature motif ($G^{43}FRxGxxP^{50}$) mediating the interaction of TF with the ribosome, is sequestered by the PPD of the other subunit in the TF dimer and thus is not available for binding to the ribosome. This finding explains why TF must monomerize upon binding to the ribosome (Ferbitz et al., 2004). The intrinsic affinity of TF for the ribosome (Kaiser et al., 2006; Maier et al., 2003) (K_d ~0.5 μM; **Figure 3-figure supplement 1*C***) is comparable to the dimerization K_d (~2 μM); therefore, there is a strong competition between TF dimerization and ribosome

202 binding. Because the affinity of TF for ribosome-nascent-chain (RNC) complexes is
203 substantially stronger (K_d <0.01 μM) (Bornemann et al., 2014; Rutkowska et al., 2008) than
204 for vacant ribosomes, translating ribosomes will be invariably bound, and thus protected by
205 TF.

206 TF uses five distinct binding sites (**Figure 3*B***) to interact with unfolded substrates
207 such as the maltose binding protein (MBP) (Saio et al., 2014). Four of these substrate-
208 binding sites are located in SBD (A-D) and the fifth one (E) is located in PPD. In the dimeric
209 form of TF only two (A and D) among these five substrate-binding sites are fully accessible
210 for binding, whereas the other three (B, C, and E) are partially occluded (**Figure 3*B***). A
211 protein substrate typically engages at least four of the binding sites (Saio et al., 2014); thus,
212 complex formation between TF and an unfolded protein requires that TF monomerize, as
213 supported by NMR and MALS data (**Figure 1-figure supplement 1** A, ***E***, and ***F***) (Saio et al.,
214 2014). Previous crystallographic data indicated that TF may also bind to small folded
215 proteins as a dimer (Martinez-Hackert and Hendrickson, 2007). However, NMR
216 characterization of such complexes in solution showed that the substrates are in an unfolded
217 state and TF is in the monomeric state (**Figure 3-figure supplement 2**).

218 Dimerization modulates the chaperone activities of TF. The concentration of TF in the cell
219 (~50 μM) is 2 to 3-fold that of the ribosome (Patzelt et al., 2002), and given the low K_d of
220 dimerization (~2 μM) the vast majority of free TF in the cytoplasm will exist in the dimeric
221 form. The dissociation rate (k_{diss}) of the dimer is ~10 s^{-1} indicating a rather dynamic TF
222 dimer with a residence time of ~100 ms (**Figure 1-figure supplement 1**G). We sought to
223 investigate whether the chaperone activity of TF is affected as it transitions between the
224 monomeric and dimeric forms. To characterize the chaperone activity of the monomeric

form of TF we used the TF^{mon} variant (**Figure 2-figure supplement 2**). The amino acid substitutions that abolish dimerization in this variant are located in RBD and thus do not affect protein substrate binding. First, we performed aggregation assay using the 35 kDa protein glyceraldehyde-3-phosphate dehydrogenase (GAPDH) in the absence and presence of TF or TF^{mon}. Denatured GAPDH was diluted into buffer and its aggregation was monitored by light scattering. The results showed that dimeric TF was substantially more efficient at suppressing aggregation than the monomeric TF (**Figure 4*A* and Figure 4-figure supplement 1**). Interestingly, decreased anti-aggregation activity of another monomeric variant, $TF^{\Delta RBD}$ (**Figure 2-figure supplement 2*E***), has also been reported previously (Merz et al., 2006). Note that the results for $TF^{\Delta RBD}$ and TF monomeric mutant are essentially identical in our GAPDH aggregation and MBP refolding assays. The anti-aggregation assay was also performed using a shorter substrate protein $OmpA^{1-192}$ (**Figure 4*B***). The results showed that in the case of the shorter substrate, which has a smaller number of hydrophobic regions (**Figure 4-figure supplement 2**), the difference in the anti-aggregation activity between the dimeric TF and

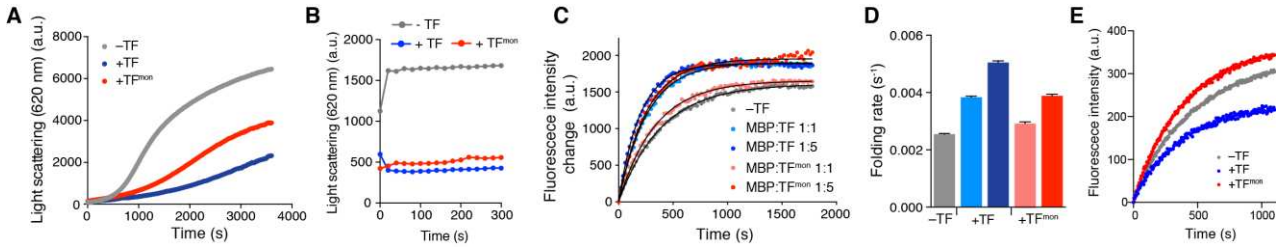

Figure 4. Effect of TF dimerization on chaperone activities. Aggregation of GAPDH in the absence or presence of TF and TF^{mon} at 0.5 μM (*A*) and OmpA in the absence or presence of TF and TF^{mon} at 4 μM (*B*). (*C*) Refolding of MBP in the absence or presence of TF and TF^{mon}. The solid line represents the fit of the data to a single exponential function. (*D*) Folding rates of MBP from the analysis of the curves shown in panel C. (*E*) Refolding of the slowly-folding MBP^{Y283D} variant in the absence or presence of TF and TF^{mon}.

monomeric TF is much less pronounced and both species are equally efficient in suppressing aggregation.

Next, we examined the efficiency of TF in assisting with the folding of MBP. Denatured MBP was diluted into buffer and its refolding was monitored by the characteristic increase in tryptophan fluorescence intensity in the absence and presence of TF or TF^{mon} (**Figure 4*C***) (Apetri and Horwich, 2008; Chakraborty et al., 2010). At 1:1 stoichiometric ratio with MBP, TF^{mon} had a minimal effect on MBP folding whereas dimeric TF had a pronounced effect (**Figure 4*C***). Specifically, dimeric TF increased the apparent folding rate of MBP and at the same time increased the yield of the soluble fraction substantially (**Figure 4 *C*** and ***D***). The increase in the apparent folding rate is likely due to the most efficient suppression of aggregation by the dimeric TF (Apetri and Horwich, 2008). Notably, a much higher TF^{mon} concentration was needed to match the chaperone activity of the dimeric TF (**Figure 4 *C*** and ***D***). We also tested the effect of TF on an aggregation-prone, slowly folding mutant of MBP (MBP^{Y283D}) (Huang et al., 2016; Saio et al., 2014). The dimeric TF was observed to have a strong "holdase" effect on the mutant MBP as evidenced by the suppression of the folding of MBP^{Y283D} (**Figure 4*E***). In contrast, TF^{mon} slightly accelerated folding (**Figure 4*E***). Because refolding of MBP^{Y283D} was performed in a chloride-free buffer in which MBP does not aggregate (Apetri and Horwich, 2008), any contribution of an anti-aggregation effect can be excluded. Taken together, all assays showed that the monomeric and dimeric TF states have distinct chaperone activities.

TF dimerization accelerates its association rate with substrates. To understand how the oligomeric state of TF affects chaperone activity, we sought to determine how the monomeric and dimeric TF species interact with protein substrates. ITC showed that TF^{mon}

has a 5-fold higher affinity (K_d ~6 μM) for protein substrates than the dimeric TF (K_d ~35 μM) (**Figure 5-figure supplement 1**). This is expected given that a sizable fraction of the substrate-binding surface is buried in the dimeric TF (**Figure 3*B*** and **Figure 5-figure supplement 2*A***). Next, we measured the kinetics of substrate binding to TF using stopped-flow fluorescence spectroscopy. Notably, the rates of protein substrate association and dissociation are very different for the dimeric (Figure 5 ***A-C***) and monomeric TF (Figure 5 ***D*** and ***E***). Specifically, unfolded PhoA binds TF^{mon} with a k_{on} ~0.5×10^6 M^{-1} s^{-1} and dissociates with a k_{off} ~6 s^{-1}. In comparison, dimeric TF binds PhoA with a 2-fold faster association rate (k_{on} ~1.1×10^6 M^{-1} s^{-1}) and dissociates with a 5-fold faster dissociation rate (k_{off} ~30 s^{-1}). The faster association of non-native proteins with the dimeric TF over the monomeric TF is consistent with the stronger holdase activity of dimeric TF (Figure 4***E***). Note that the holdase activity of a chaperone is determined by the difference between the folding rate of the substrate protein and the association rate between the chaperone and the unfolded substrate protein, as shown by kinetic experiments on SecB and TF (Huang et al., 2016). Thus the association rate of dimeric TF for the substrate appears to be fast enough to delay the folding of the slowly folding mutant MBP^{Y283D}, but not fast enough to delay the folding of wild type MBP (Figure 4 ***C*** and ***E***). Although three out of the five substrate-binding sites are partially occluded in the dimeric TF, assembly of the dimer brings next to each other substrate-binding sites A, B, and D in the two subunits. The sites are located within a large cavity that is accessible to unfolded proteins (**Figure 5-figure supplement 2**) and present to the substrate a large contiguous binding surface that may account for the enhanced association rates of substrates with the dimeric TF.

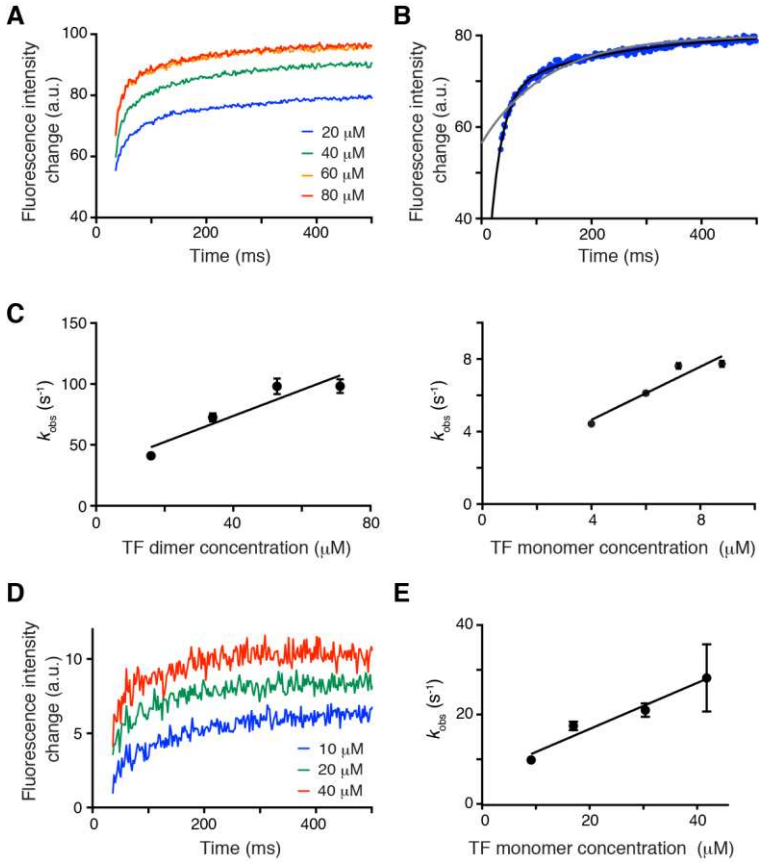

Figure 5. Effect of TF dimerization on binding kinetics. (*A*) Association of unfolded PhoA with TF monitored by tryptophan fluorescence. (*B*) Fitting of the data for the association of PhoA with TF by a single exponential function (gray line) or the sum of two exponential functions (black line), indicating that two exponential functions are required to fit the data. (*C*) Plots of the observed rate constant (k_{obs}) as a function of the concentration of the dimer (left) and the monomer (right) of TF. (*D*) Association of PhoA with TF^{mon} monitored by tryptophan fluorescence. (*E*) Plot of the observed rate constant (k_{obs}) as a function of the concentration of monomeric TF.

284

285 Discussion

286 Our findings demonstrate how changes in the oligomerization state of a molecular
287 chaperone may modulate the folding properties to interacting substrate proteins. The
288 structural, energetic and kinetic data presented here explain previous observations and offer
289 new insights into the various roles of TF in the cytoplasm (Figure 6). When bound to the
290 ribosome (Figure 6, panel i), TF is in the monomeric form and exposes all substrate-binding

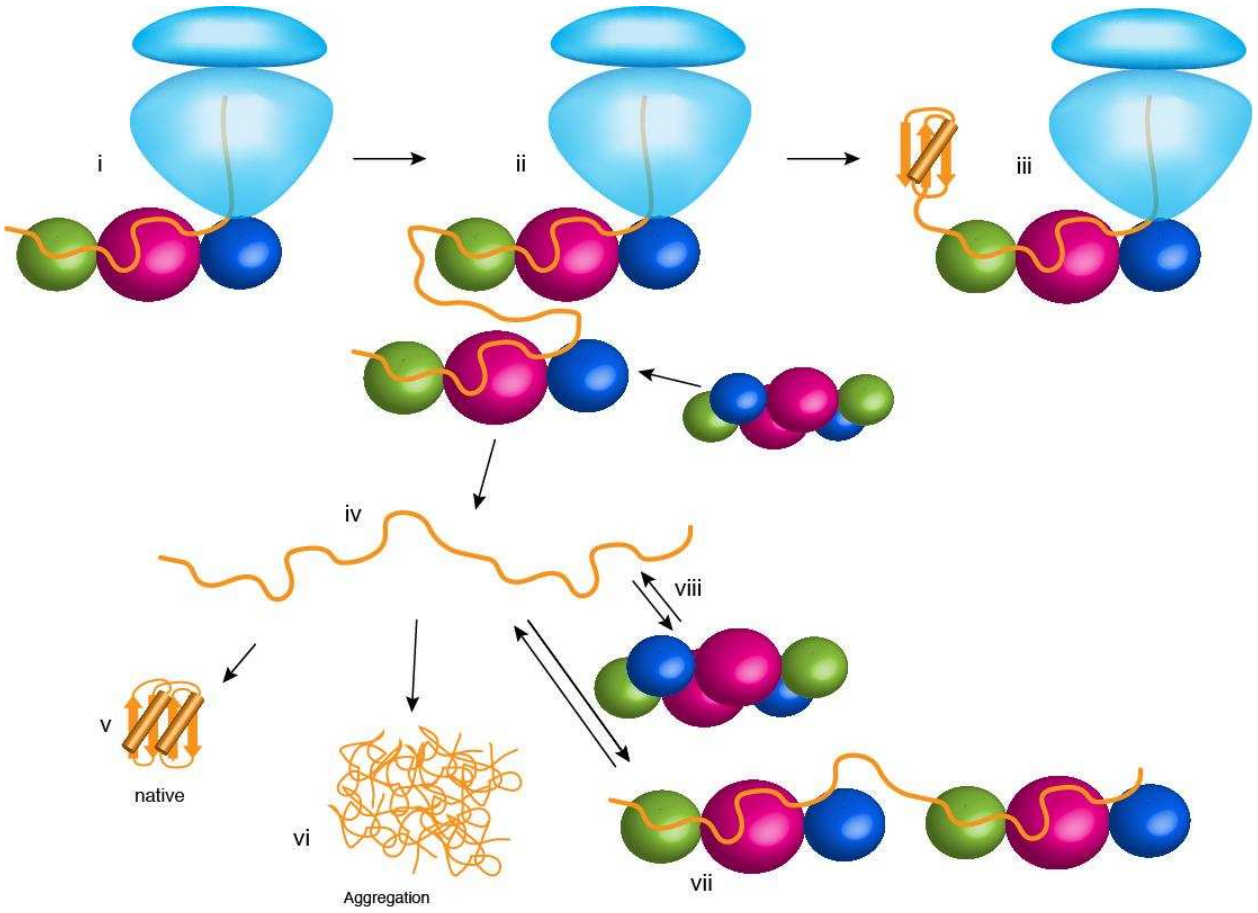

Figure 6. Chaperone activities of TF in the cell. The ribosome is shown in light blue. The protein substrate is shown in orange, and TF is represented as spheres with the subunits colored as in Figure 2A. See text for details.

sites to the nascent protein. The co-localization with the nascent chain results in TF delaying folding and preventing aggregation as shown before (Agashe et al., 2004; Hoffmann et al., 2012; O'Brien et al., 2012; Saio et al., 2014). As the nascent chain grows, additional TF molecules are recruited (Figure 6, panel ii) (Kaiser et al., 2006). Because of the high concentration of free TF in the cytoplasm, it is likely that a TF molecule outcompetes and displaces the fraction of the nascent chain that is bound to the TF to form a TF dimer. In this case, folding of a domain may occur co-translationally (Figure 6, panel iii). Most cytosolic proteins released from the ribosome (Figure 6, panel iv) spontaneously form their native structure (Balchin et al., 2016) (Figure 6, panel v). However, in the absence of molecular chaperones, many proteins have a tendency to aggregate (Figure 6, panel vi). TF has an anti-aggregation activity, with the dimeric form being more potent than the monomeric form (Figure 4 ***A*** and ***C***). We posit that this is because of the higher local concentration of TF subunits in the dimeric form, which can both bind upon dimer dissociation with the interacting non-native polypeptide to protect longer segments of the polypeptide (Figure 6, panel vii). The increased local concentration of TF subunits results in faster association of the second molecule of TF to the substrate protein, which enables TF to more efficiently capture the substrate protein before the it starts to aggregate. This hypothesis is consistent with the following findings: (i) higher concentrations of monomeric TF are needed to achieve the same anti-aggregation activity as the dimeric TF (Figure 4C); and (ii) aggregation of shorter substrates, which are expected to bind to a single TF molecule, are equally prevented by the monomeric and dimeric TF (Figure 4B). Depending on the energetics and kinetics of interaction between TF and the non-native polypeptide in the cytoplasm, dimeric TF can also function as a potent holdase chaperone (Figure 4E) to delay

314 the folding of proteins destined for export, such as periplasmic and outer membrane
315 proteins (Oh et al., 2011). Our findings demonstrate how the activity of a chaperone can be
316 modulated and tailored to specialized needs in the cell simply by a change in the oligomeric
317 state of the chaperone, without the need of ATP binding and hydrolysis cycles or the binding
318 of co-factors.

Materials and methods

Key resources table

Reagent type (species) or resource	Designation	Source or reference	Identifiers
strain, strain background (*E. coli*)	BL21 (DE3)	NIPPON GENE CO., LTD.	ECOS Competent E. coli BL21 (DE3)
recombinant DNA reagent	PhoA	Saio et al. 2014, Science PMID: 24812405	NCBIGene:945041
recombinant DNA reagent	OmpA	Tsirigotaki et al. 2018, Structure doi: 10.1016/j.str.2018.03.006.	NCBIGene:945571
recombinant DNA reagent	RT	Inouye et al. 1999, J. Biol. Chem. PMID: 10531319	UniProtKB: P23070
recombinant DNA reagent	MBP	Huang et al. 2016, Nature PMID: 27501151	NCBIGene: 948538
recombinant DNA reagent	TF	Takara Bio inc.	pCold-TF (TKR 3365)
S7	S7	GenScript	Gene synthesis
peptide, recombinant protein	GAPDH	Sigma-Aldrich	G-2267
software, algorithm	CYANA3.97	Guntert 2004, Methods Mol Biol. PMID: 15318003	RRID:SCR_014229
software, algorithm	CNS	Brunger 2007, Nat Protoc. PMID: 18007608	RRID:SCR_014223

Sample preparation. The *E. coli* TF, RBD (residues 1 to 117), PPD (residues 148 to 249), SBD (residues 113–432Δ150–246), $TF^{\Delta RBD}$ (residues 113 to 246), $TF^{\Delta PPD}$ (residues 1–432Δ150–243), $OmpA^{1-192}$, and PhoA were expressed and purified as described previously (Saio et al., 2014). TF, PPD, $TF^{\Delta RBD}$, and $TF^{\Delta PPD}$ were cloned into the pCold vector (Takara Bio). RBD and SBD were cloned into pET16b vector (Novagen) and fused to His_6-MBP and a tobacco etch virus (TEV) protease cleavage site. TF mutants were constructed by site-directed mutagenesis using PfuTurbo High Fidelity DNA

polymerase (Agilent) as well as PrimeSTAR Max (Takara Bio). OmpA$^{1\text{-}192}$ was fused with N-terminal His$_6$-tag and cloned into pET16b. Precursor form of maltose-binding protein (preMBP) and MBP^{Y283D} were expressed and purified as described previously (Huang et al., 2016). *E. coli* reverse transcriptase (RT)-Ec86 255-320 was cloned into pCold-TF (Takara Bio) including a ~25 a.a. linker between TF and RT. *E. coli* S7 was cloned into pET16b vector and fused to His$_6$-MBP, including a tobacco etch virus (TEV) protease cleavage site. All constructs were transformed into *E. coli* BL21 (DE3) cells.

For the unlabeled protein samples, cells were grown in Luria-Bertani (LB) medium at 37°C in the presence of ampicillin (100 mg L^{-1}). Protein expression was induced by the addition of 0.2 to 0.5 mM isopropyl-β-D-1-thiogalactopyranoside (IPTG) at OD_{600} ~0.6, followed by ~16 hours of incubation at 18 °C. For isotopically labeled samples for NMR studies, cells were grown in minimal (M9) medium at 37°C in the presence of ampicillin (100 mg L^{-1}). Protein expression was induced by the addition of 0.2 to 0.5 mM IPTG at OD_{600} ~0.6, followed by ~16 hours of incubation at 18°C. The samples with ^{1}H,^{13}C-labeled methyl and aromatic side chains in deuterium background were prepared as described previously (Saio et al., 2014). The cells were grown in medium with $^{15}NH_4Cl$ (1 gL^{-1}) and $^{2}H_7$-glucose (2 gL^{-1}) in 99.9% $^{2}H_2O$ (CIL and Isotec). For preparation of ^{1}H-^{13}C methyl-labeled samples, α-ketobutyric acid (50 mg L^{-1}) and α-ketoisovaleric acid (85 mg L^{-1}), [$^{13}CH_3$] methionine (50 mg L^{-1}), [$^{2}H_2$, $^{13}CH_3$] alanine (50 mg L^{-1}) were added to the culture 1 hour before the addition of IPTG. For Phe and Tyr labeling, U-[^{1}H, ^{13}C]-labeled amino acids were added to the culture 1 hour before the addition of IPTG.

Cells were harvested and resuspended in the lysis buffer containing 50 mM Tris-HCl pH 8.0, 500 mM NaCl. Cells were disrupted by a high-pressure homogenizer or sonicator and centrifuged at 50,000 g for 45 min. TF, TF variants, and PhoA fragments were purified using Ni Sepharose 6 Fast Flow resin (GE Healthcare). In the case of RBD, SBD, and PhoA fragments that contain TEV cleavage site, the His_6-MBP tag was removed by TEV protease at 4°C (incubation for 16 hours). The proteins were further purified by gel filtration using Superdex 75 16/60 or 200 16/60 columns (GE Healthcare). TF-RT complex was purified using Ni Sepharose 6 Fast Flow resin, followed by gel filtration using Superdex 200 16/60 column equilibrated with a solution containing 20 mM potassium phosphate (pH 7.0), 100 mM KCl, 4 mM β-mercaptoethanol, 0.5 mM EDTA, 0.05% NaN_3. S7 was purified using Ni Sepharose 6 Fast Flow resin, followed by the removal of His_6-MBP tag by TEV protease digestion at 4°C in the presence of TF. TF-S7 complex was further purified by gel filtration using Superdex 200 16/60 column equilibrated with a solution containing 20 mM potassium phosphate (pH 7.0), 100 mM KCl, 4 mM β-mercaptoethanol, 0.5 mM EDTA, 0.05% NaN_3. MBP^{Y283D} and preMBP was purified using Ni Sepharose 6 Fast Flow resin, followed by gel filtration using Superdex 200 16/60 column equilibrated with a solution containing 100 mM HEPES, pH 7.5, 20 mM potassium acetate, 5 mM magnesium acetate. For $OmpA^{1-192}$, the cell pellet was resuspended in a solution containing 50 mM Tris-HCl (pH 8.0), 500 mM NaCl, and 8 M urea and incubated for 1 hour at room temperature, followed by centrifugation at 50,000g for 45 min. The solubilized protein was purified using Ni Sepharose 6 Fast Flow resin, and eluted with a solution containing 50 mM Tris-HCl (pH 8.0), 500 mM NaCl, 400 mM imidazole, and 8 M urea.

NMR spectroscopy. For NMR titrations and NOE measurement, NMR samples were prepared in 20 mM potassium phosphate (pH 7.0), 100 mM KCl, 4 mM β-mercaptoethanol, 0.5 mM EDTA, 0.05% NaN_3, and 7% ^2H_2O. The proteins were concentrated to 0.3 ~ 2.2 mM for NOESY measurements. NMR spectra were recorded on Agilent UNITY Inova 600 and 800 MHz NMR spectrometers and Bruker Avance III 600, 700, and 800 MHz NMR spectrometers. Bruker Avance III 700 was equipped with cryogenic probe. The experiments were run at 10, 22, and 35°C. Spectra were processed using the NMRPipe program (Delaglio et al., 1995), and data analysis was performed with Olivia (fermi.pharm.hokudai.ac.jp/olivia). NOE distance restraints for the dimer was collected by ^{13}C-edited NOESY-HMQC, 3D (^1H)-^{13}C HMQC-NOESY-^1H-^{13}C HMQC, 3D-SOFAST-(^1H)-^{13}C HMQC-NOESY-^1H-^{13}C HMQC and ^{13}C-edited SOFAST-NOESY-HMQC (Rossi et al., 2016) recorded on [U-^2H; Ala-$^{13}CH_3$; Met-$^{13}CH_3$; Ile-δ1-$^{13}CH_3$; Leu/Val-$^{13}CH_3$/$^{13}CH_3$; Phe-$^{13}C^{15}N$; Tyr-$^{13}C^{15}N$]-labeled TF or on 1:1 mixture of [U-^2H; Ala-$^{13}CH_3$; Met-$^{13}CH_3$; Ile-δ1-$^{13}CH_3$]-labeled TF and [Leu/Val-$^{13}CH_3$/$^{13}CH_3$; Phe-$^{13}C^{15}N$; Tyr-$^{13}C^{15}N$]-labeled TF. The 1:1 mixture of the TF proteins with different labeling schemes enabled us to unambiguously identify the intermolecular NOEs: For example, an NOE observed between Ile and Leu can be unambiguously classified as an intermolecular NOE. Although the resonances from the interface, especially from RBD, undergo severe line broadening, high sensitivity of methyl resonances in deuterated background as well as high solubility and stability of TF at wide range of temperature enabled observation of substantial number of NOEs. NOEs were further collected by 3D (^1H)-^{13}C HMQC-NOESY-^1H-^{13}C HMQC, 3D-SOFAST-(^1H)-^{13}C HMQC-NOESY-^1H-^{13}C HMQC, and ^{13}C-edited SOFAST-NOESY-HMQC recorded on [U-^2H; Ala-$^{13}CH_3$; Met-$^{13}CH_3$; Ile-δ1-$^{13}CH_3$; Leu/Val-

$^{13}CH_3/^{13}CH_3$; Phe-$^{13}C^{15}N$; Tyr-$^{13}C^{15}N$]-labeled RBD in complex with [U-^{2}H; Ala-$^{13}CH_3$; Met-$^{13}CH_3$; Ile-δ1-$^{13}CH_3$; Leu/Val-$^{13}CH_3/^{13}CH_3$]-labeled $TF^{\Delta RBD}$. To corroborate intra-molecular distance restraints, 3D (^{1}H)-^{13}C HMQC-NOESY-^{1}H-^{13}C HMQC, 3D (^{1}H)-^{15}N HMQC-NOESY-^{1}H-^{13}C HMQC, 3D (^{1}H)-^{13}C HMQC-NOESY-^{1}H-^{15}N HMQC, ^{13}C-edited NOESY-HMQC, ^{13}C-edited NOESY-HSQC, ^{13}C-edited HSQC-NOESY, ^{15}N-edited NOESY-HMQC, and ^{15}N-edited NOESY-HSQC were recorded on [U-^{2}H; Ala-$^{13}CH_3$; Met-$^{13}CH_3$; Ile-δ1-$^{13}CH_3$; Leu/Val-$^{13}CH_3/^{13}CH_3$; Phe-$^{13}C^{15}N$; Tyr-$^{13}C^{15}N$]-labeled RBD, [U-^{2}H; Ala-$^{13}CH_3$; Met-$^{13}CH_3$; Ile-δ1-$^{13}CH_3$; Leu/Val-$^{13}CH_3/^{13}CH_3$; Phe-$^{13}C^{15}N$; Tyr-$^{13}C^{15}N$]-labeled SBD, or $^{13}C^{15}N$-labeled PPD.

Paramagnetic Relaxation Enhancement experiment. To observe paramagnetic relaxation enhancement (PRE), nitroxide spin label 1-oxyl-2,2,5,5-tetramethyl-3-pyrroline-3-methyl)-ethanethiosulfonate (MTSL, Toronto Research Chemicals Inc.) were introduced via cysteine-specific modification of TF K46C. Wild type TF has no cysteine residues. K46 mutant and its MTSL derivatives were determined not to perturb the TF structure, as assessed by ^{1}H-^{13}C HMQC spectra. After purification, [U-^{2}H; Met-$^{13}CH_3$; Ile-δ1-$^{13}CH_3$; Leu/Val-$^{13}CH_3/^{13}CH_3$]-labeled TF K46C was exchanged into tris buffer (50 mM Tris-HCl pH 7.0, 50 mM KCl, and 1 mM β-mercaptoethanol). β-mercaptoethanol was removed by Zeba spin desalting column (Thermo Scientific) according to the manufacturer's protocol. MTSL was added from a concentrated stock in acetonitrile at a 10-fold excess, and the reaction was allowed to proceed at 4 °C for ~12h. Excess MTSL was extensively removed by an Amicon stirred cell. PREs were observed from ^{1}H-^{13}C HMQC spectra of TF in the absence and presence of PhoA by measuring peak intensities before

(paramagnetic) and after (diamagnetic) reduction of the nitroxide spin label with ascorbic acid.

Structure determination of TF dimer. The resonances of the full-length dimeric TF (~100 kDa) were assigned by a domain-parsing approach as reported previously (Saio et al., 2014). Near-complete assignment of TF was achieved for the resonances from methyl side chain, aromatic side chain, and amide group. The structure of TF dimer was calculated by CYANA 3.97 (Guntert, 2004) using the NOE-derived distance restraints, dihedral angle-restraints, and hydrogen bond restraints. PREs were solely used to monitor TF monomerization upon the addition of the substrate protein (Figure 1-figure supplement 1A), and were not used in the structure calculation. NOE peak lists were obtained from 3D (^{1}H)-^{13}C HMQC-NOESY-^{1}H-^{13}C HMQC, 3D (^{1}H)-^{15}N HMQC-NOESY-^{1}H-^{13}C HMQC, 3D (^{1}H)-^{13}C HMQC-NOESY-^{1}H-^{15}N HMQC, 3D-SOFAST-(^{1}H)-^{13}C HMQC-NOESY-^{1}H-^{13}C HMQC and ^{13}C-edited SOFAST-NOESY-HMQC, ^{13}C-edited NOESY-HMQC, ^{13}C-edited NOESY-HSQC, ^{13}C-edited HSQC-NOESY, ^{15}N-edited NOESY-HMQC, and ^{15}N-edited NOESY-HSQC. Substantial number of inter- and intra-molecular NOEs were observed from NOESY spectra recorded on full length TF. The NOE restraints were further corroborated by the NOEs observed from isolated RBD in complex with TF$^{\Delta RBD}$. The chemical shift perturbation profiles as well as NOEs observed for RBD-TF$^{\Delta RBD}$ complex were consistent with those observed for full length TF, supporting the idea that the binding mode in the TF dimer is preserved in the interaction between the isolated domains. The intramolecular restraints obtained from NOESY experiments on full length TF were also corroborated by NOEs observed from the isolated domains of PPD, SBD and RBD. Note that most of the intramolecular NOEs from the isolated

442 domains were consistent with the NOEs observed from TF dimer. A few intra-molecular
443 NOEs observed from the isolated domains especially from the regions close to the
444 dimer interface and the hinge regions were excluded in the calculation. Accordingly
445 more than 2,500 intramolecular NOEs as well as 54 intermolecular NOEs were collected
446 for structure calculation (Table 1) (Figure 2-figure supplement 4). NOE restraints were
447 corroborated by dihedral angle restraints derived from TALOS+ (Shen et al., 2009) and
448 hydrogen bond restraints added for the regions forming secondary structures as judged
449 by the NOEs and TALOS+-derived dihedral angles. Intermolecular hydrogen bond
450 restraints were added for the pair of atoms located close in the majority of the
451 conformers in the NOE-derived preliminary structure. For the core region of RBD
452 remote to the dimer interface, distance restraints from the crystal structure (Ferbitz et
453 al., 2004) were loosely added to maintain overall fold of RBD. The 20 lowest-energy
454 structures resulted from CYANA calculation were refined by restrained molecular
455 dynamics in explicit water with CNS (Brunger, 2007). All of the intermolecular NOEs
456 were well satisfied in the structure. The coordinates, restraints, chemical shift
457 assignments have been deposited to PDB and BMRB.

458 **SEC-MALS experiments.** Size-exclusion chromatography with multi-angle light
459 scattering (SEC-MALS) was measured using DAWN HELEOS-II (Wyatt Technology
460 Corporation) downstream of a Shimadzu liquid chromatography system connected to
461 Superdex 200 10/300 GL (GE Healthcare) gel filtration column, or using DAWN
462 HELEOS8+ (Wyatt Technology Corporation) downstream of TOSOH liquid
463 chromatography system connected to TSKgel G3000SWXL (TOSOH Corporation) gel
464 filtration column. In both instruments, the differential refractive index (Shimadzu

Corporation) downstream of MALS was used to obtain protein concentration. The running buffer was 20 mM potassium phosphate (pH 7.0), 100 mM KCl, 4 mM β-mercaptoethanol, and 0.5 mM EDTA. 100 ~ 200 µL of the sample was injected with a flow rate of 0.5 ~ 1.0 mL min^{-1}. The data were analyzed with ASTRA version 6.0.5 or 7.0.1 (Wyatt Technology Corporation). To obtain the dissociation constant (K_d) of TF dimer, TF was injected at varying concentrations, followed by K_d estimation based on the weight-averaged molar mass as determined by SEC-MALS and protein concentration at the peak top, using the following equation.

$$M_w = M_m \left(\frac{8[M]_T + K_d - \sqrt{K_d^2 + 8[M]_T K_d}}{4[M]_T} \right) \qquad (1)$$

where M_w is the weight average molar mass obtained by SEC-MALS, $[M]_T$ is the molar concentration of protein (as measured by change in refractive index), and M_m is molecular mass of the monomer. Nonlinear least square fitting was performed using Prism 5 (GraphPad Software).

Analytical ultracentrifugation experiments. Sedimentation velocity experiments were conducted in a ProteomeLab XL-I analytical ultracentrifuge (Beckman Coulter, Indianapolis, IN) following standard protocols unless mentioned otherwise (Benfield et al., 2011). The samples, dialyzed overnight against the reference buffer (50 mM sodium phosphate pH 7.0, 100 mM NaCl) were loaded into a cell assembly comprised of a double sector charcoal-filled centerpiece with a 12 mm path length and sapphire windows. Buffer density and viscosity were determined in a DMA 5000 M density meter and an AMVn automated micro-viscometer (both Anton Paar, Graz, Austria), respectively. The partial specific volumes and the molecular masses of the proteins

were calculated based on their amino acid compositions in SEDFIT (https://sedfitsedphat.nibib.nih.gov/software/default.aspx). The cell assembly, containing identical sample and reference buffer volumes of 360 µL, was placed in a rotor and temperature equilibrated at rest at 20 °C for 2 hours before it was accelerated from 0 to 50,000 rpm. Absorbance scans at 230 and 280 nm were collected continuously for 12 hours. The velocity data were modeled with diffusion-deconvoluted sedimentation coefficient distributions c(s) in SEDFIT (https://sedfitsedphat.nibib.nih.gov/software/default.aspx), using algebraic noise decomposition and with signal-average frictional ratio and meniscus position refined with non-linear regression. The s-values were corrected for time and finite acceleration of the rotor was accounted for in the evaluation of Lamm equation solutions (Benfield et al., 2011). Maximum entropy regularization was applied at a confidence level of P-0.68.

Sedimentation velocity isotherm data i.e. the signal-weighted average sedimentation coefficients, sw(c), of the total sedimenting system derived from integration of the complete c(s) distributions at various concentrations (40.18, 12.13, 3.83 and 0.596 µM) of TF were fitted to a monomer-dimer self-association model using SEDPHAT (https://sedfitsedphat.nibib.nih.gov/software/default.aspx). For interacting systems, sw represents the average sedimentation property of the species under investigation. The association scheme used in this analysis was A + A ↔ A2 with equilibrium dissociation constant K_d. All plots were generated with the program GUSSI (kindly provided by Dr. Chad Brautigam).

Stopped-flow experiments. Kinetic measurements were performed on FP-8300 Fluorescence Stopped Flow System (JASCO Corporation). The excitation and emission wavelengths were set at 280 nm (band width 10 nm) and 350 nm (band width 20 nm), respectively, so that the intrinsic tryptophan-fluorescence of $PhoA^{220-310}$ containing two Trp residues or that of TF containing one tryptophan residue can be monitored. All measurements were carried out in the buffer containing 20 mM potassium phosphate (pH 7.0), 100 mM KCl, 4 mM β-mercaptoethanol, 0.5 mM EDTA, 0.05% NaN_3. Individual kinetics were typically measured 40 times and averaged. The data was analyzed with Prism 5 (GraphPad Software). To account for photobleaching, an exponential baseline was defined using the data after 1000 ms of the mixing, by which the dissociation or association has completed and reached to the equilibrium. Dissociation of TF dimer was initiated by 10-fold dilution of TF at 1 μM. The temperature was set to 22°C. The protein solution was placed in 2.5 mL syringe and the buffer was placed in 10 mL syringe. The dissociation kinetics was analyzed using a single exponential function. Binding between TF and $PhoA^{220-310}$ was monitored after rapid mixing by the stopped-flow instrument. Association of $PhoA^{220-310}$ and TF or TF^{mon} was initiated by mixing equal volumes of 4 μM PhoA220-310 and 0-80 μM TF or TF^{mon} resulting in final concentrations of 2 μM $PhoA^{220-310}$ and 0-40 μM TF or TF^{mon}. A single tryptophan residue in TF (W151) was mutated to phenylalanine in order to selectively monitor the change in the fluorescence from $PhoA^{220-310}$ containing two residues both located in the binding sites for TF (Saio et al., 2014). Both samples were placed in the 10 mL syringe. The temperature was set to 18°C. The fluorescence intensity of $PhoA^{220-310}$ increased upon binding to TF as seen in the previous report using reduced and carboxymethylated form of α-lactalbumin

(RCM-La). When PhoA$^{220\text{-}310}$ was mixed with the monomeric mutant TF^{mon}, each of the time traces was well explained by a single exponential curve. The time traces at varying concentration of TF^{mon} showed linear dependence of the observed rate k_{obs} on the concentration of TF^{mon}, and k_{on} and k_{off} were extracted by fit of the data to the linear function of $k_{obs} = k_{on}[TF] + k_{off}$. On the other hand, the time traces of the binding between PhoA$^{220\text{-}310}$ and TF were best represented as the sum of the two exponential curves. The fit of the time traces to two exponential functions resulted the fraction of the fast phase more than 80% that increased as the concentration of TF increased. The fraction for the fast phase coincides with the fraction of the dimer as estimated by the K_d of dimerization (2 μM) determined by the AUC experiment, and thus we concluded that the fast and slow phases are attributed to the binding of PhoA$^{220\text{-}310}$ to the dimer and the monomer fractions of TF, respectively. The concentration for the plots of k_{obs} was calculated for each of the dimer and the monomer, using the K_d of dimerization (2 μM). The kinetic parameters determined for the monomer fraction of TF roughly correspond to those determined for the monomeric mutant TF^{mon}.

ITC experiments. For the ribosome and TF, calorimetric titrations were carried out on iTC200 microcalorimeter (GE healthcare) at 22°C. All protein samples were dialyzed against ITC buffer containing 20 mM HEPES, pH 7.5, 50 mM potassium acetate, 20 mM $MgCl_2$, and 1 mM tris(2-carboxyethyl)phosphine (TCEP). The 200 μL sample cell was filled with 12 μM solution of the ribosome, and 40 μL injection syringe was filled with 160 to 190 μM solution of TF or RBD. The titrations were carried out with a preliminary 0.2 μL injection, followed by 14 injections of 2.5 μL each with time intervals of 5 min. The solution was stirred at 1000 rpm. For unfolded substrates (PhoA$^{220\text{-}310}$ or MBP$^{198\text{-}}$

^{265}) and TF, TF^{mon}, or TF$^{\Delta RBD}$, calorimetric titrations were carried out on Auto-iTC200 microcalorimeter (GE healthcare). The calorimetric titrations for PhoA220-310 and MBP198-265 were performed at 8°C and 22°C, respectively. All protein samples were purified in ITC buffer containing 20 mM potassium phosphate (pH 7.0), 100 mM KCl by gel filtration. For titration of PhoA$^{220-310}$, the 200 μL sample cell was filled with 90 μM solution of TF, TF^{mon}, or TF$^{\Delta RBD}$, and 40 μL injection syringe was filled with 1.1 mM solution of PhoA$^{220-310}$. For titration of MBP$^{198-265}$, the 200 μL sample cell was filled with 110 μM solution of TF or TF$^{\Delta RBD}$, and 40 μL injection syringe was filled with 1.1 mM solution of MBP198-265. The titrations were carried out with a preliminary 0.2 μL injection, followed by 8 injections of 4.2 μL each with time intervals of 5 min. The solution was stirred at 1000 rpm. Data for the preliminary injection, which are affected by diffusion of the solution from and into the injection syringe during the initial equilibration period, were discarded. Binding isotherms were generated by plotting heats of reaction normalized by the modes of injectant versus the ratio of total injectant to total protein per injection. The data were fitted with Origin 7.0 (OriginLab Corporation, Northampton, MA).

Anti-aggregation assays. Aggregation of denatured GAPDH from rabbit muscle (Sigma; G-2267) was measured as described previously (Saio et al., 2014). 125 μM GAPDH was denatured by 3 M guanidine-HCl in 20 mM potassium phosphate, pH 7.0, 100 mM KCl, 4 mM β-mercaptoethanol, 0.5 mM EDTA, and 0.05% NaN_3 for 12 h at 4 °C. The denatured GAPDH was diluted 50-fold into the buffer that does not contain guanidine-HCl and aggregation was monitored by 90° light scattering at 620 nm on a spectrofluorometer (FP-8500, JASCO Corporation) in the absence or presence of TF or TF^{mon} at the

concentration of 0.5 μM or 1 μM. The experiment was carried out at 20°C. The reproducibility was confirmed by independent assays repeated three times.

In anti-aggregation assay on $OmpA^{1-192}$, 62 μM $OmpA^{1-192}$ in 50 mM Tris-HCl pH 8.0, 500 mM NaCl, 400 mM imidazole, and 8 M urea was diluted 20-fold into 20 mM potassium phosphate, pH 7.0, 100 mM KCl, 4 mM β-mercaptoethanol, 0.5 mM EDTA, and 0.05% NaN_3. Aggregation was monitored by 90° light scattering at 620 nm on a spectrofluorometer (FP-8500, JASCO Corporation) in the absence or presence of TF or TF^{mon} at the concentration of 4 μM. The experiment was carried out at 25°C.

MBP refolding assay. Refolding experiments of the precursor form of MBP, preMBP, and slower folding mutant, MBP^{Y283D}, were performed as described before (Huang et al., 2016) with some modifications. The proteins were denatured in the buffer containing 100 mM HEPES, pH 7.5, 20 mM potassium acetate, 5 mM magnesium acetate, and 8 M urea. PreMBP and MBP^{Y283D} were concentrated to 80 and 32 μM, respectively. Refolding of preMBP was initiated by 20-fold rapid dilution into the buffer containing 50 mM sodium phosphate, pH 7.0, 150 mM NaCl, and 0.05% NaN_3. Refolding process of preMBP in the absence and presence of TF or $TF^{\Delta RBD}$ at the concentration of 4 or 20 μM was monitored by an increase in tryptophan fluorescence intensity. Fluorescence intensity was measured using a microplate reader (Infinite 200 PRO, Tecan). The excitation and emission wavelengths were set at 295 nm (band width 5 nm) and 335 nm (band width 20 nm), respectively. The refolding was performed three times and averaged. All measurements were performed at 25°C. Data were analyzed by Prism 5 (GraphPad Software) using single exponential function. Refolding of MBP^{Y283D} was initiated by 20-fold rapid dilution into the buffer containing 100 mM HEPES, pH 7.5, 20 mM potassium

601 acetate, 5 mM magnesium acetate and the refolding process of MBP^{Y283D} in the absence
602 and presence of TF or TF^{mon} at the concentration of 10 or 20 μM was monitored by an
603 increase in tryptophan fluorescence intensity. Fluorescence intensity was measured
604 using a spectrofluorometer (FP-8500, JASCO Corporation). The excitation and emission
605 wavelengths were set at 295 nm (band width 2.5 nm) and 335 nm (band width 5 nm),
606 respectively. The refolding was performed three times and averaged. All measurements
607 were performed at 25°C.

608

609 Acknowledgements

610 We thank P. Rossi (St. Jude Children's Research Hospital), H. Kumeta (Hokkaido
611 University), Y. Kumaki (Hokkaido University), Y. Xia (St. Jude Children's Research
612 Hospital), and S. Kim (Rutgers University) for their help with setting up NMR
613 experiments, K. Maenaka (Hokkaido University) and Center for Research and Education
614 on Drug Discovery for the use of iTC200, M. Inouye (Robert Wood Johnson Medical
615 School) for providing the RT expression plasmid. This work was supported by National
616 Institutes of Health grant GM122462 (to C.G.K) and by JSPS KAKENHI (17H05657) and
617 PRESTO JST (to T.S.). Some of the NMR experiments were performed at Hokkaido
618 University Advanced NMR Facility, a member of NMR Platform.

619

620 Competing interests

621 The other authors have declared that no competing interests exist.

622

623 References

624 Agashe, V.R., Guha, S., Chang, H.-C., Genevaux, P., Hayer-Hartl, M., Stemp, M., Georgopoulos,
625 C., Hartl, F.U., and Barral, J.M. (2004). Function of trigger factor and DnaK in multidomain protein
626 folding: increase in yield at the expense of folding speed. Cell *117*, 199-209.
627 Apetri, A.C., and Horwich, A.L. (2008). Chaperonin chamber accelerates protein folding through
628 passive action of preventing aggregation. Proc Natl Acad Sci U S A *105*, 17351-17355.
629 Balchin, D., Hayer-Hartl, M., and Hartl, F.U. (2016). In vivo aspects of protein folding and quality
630 control. Science *353*, aac4354.
631 Benfield, C.T., Mansur, D.S., McCoy, L.E., Ferguson, B.J., Bahar, M.W., Oldring, A.P., Grimes,
632 J.M., Stuart, D.I., Graham, S.C., and Smith, G.L. (2011). Mapping the IkappaB kinase beta
633 (IKKbeta)-binding interface of the B14 protein, a vaccinia virus inhibitor of IKKbeta-mediated
634 activation of nuclear factor kappaB. J Biol Chem *286*, 20727-20735.
635 Bornemann, T., Holtkamp, W., and Wintermeyer, W. (2014). Interplay between trigger factor
636 and other protein biogenesis factors on the ribosome. Nat Commun *5*, 4180.
637 Brunger, A.T. (2007). Version 1.2 of the Crystallography and NMR system. Nat Protoc *2*, 2728-
638 2733.
639 Bukau, B., Weissman, J., and Horwich, A. (2006). Molecular chaperones and protein quality
640 control. Cell *125*, 443-451.
641 Chakraborty, K., Chatila, M., Sinha, J., Shi, Q., Poschner, B.C., Sikor, M., Jiang, G., Lamb, D.C.,
642 Hartl, F.U., and Hayer-Hartl, M. (2010). Chaperonin-catalyzed rescue of kinetically trapped states
643 in protein folding. Cell *142*, 112-122.
644 Clare, D.K., Vasishtan, D., Stagg, S., Quispe, J., Farr, G.W., Topf, M., Horwich, A.L., and Saibil,
645 H.R. (2012). ATP-triggered conformational changes delineate substrate-binding and -folding
646 mechanics of the GroEL chaperonin. Cell *149*, 113-123.
647 Crooke, E., Guthrie, B., Lecker, S., Lill, R., and Wickner, W. (1988). ProOmpA is stabilized for
648 membrane translocation by either purified E. coli trigger factor or canine signal recognition
649 particle. Cell *54*, 1003-1011.
650 Delaglio, F., Grzesiek, S., Vuister, G.W., Zhu, G., Pfeifer, J., and Bax, A. (1995). NMRPipe: a
651 multidimensional spectral processing system based on UNIX pipes. J Biomol NMR *6*, 277-293.
652 Eyles, S.J., and Gierasch, L.M. (2010). Nature's molecular sponges: small heat shock proteins
653 grow into their chaperone roles. Proc Natl Acad Sci U S A *107*, 2727-2728.
654 Ferbitz, L., Maier, T., Patzelt, H., Bukau, B., Deuerling, E., and Ban, N. (2004). Trigger factor
655 in complex with the ribosome forms a molecular cradle for nascent proteins. Nature *431*, 590-596.
656 Guntert, P. (2004). Automated NMR structure calculation with CYANA. Methods Mol Biol *278*,
657 353-378.
658 Haldar, S., Tapia-Rojo, R., Eckels, E.C., Valle-Orero, J., and Fernandez, J.M. (2017). Trigger
659 factor chaperone acts as a mechanical foldase. Nat Commun *8*, 668.
660 Hayer-Hartl, M., Bracher, A., and Hartl, F.U. (2016). The GroEL-GroES Chaperonin Machine: A
661 Nano-Cage for Protein Folding. Trends Biochem Sci *41*, 62-76.
662 He, L., Sharpe, T., Mazur, A., and Hiller, S. (2016). A molecular mechanism of chaperone-client
663 recognition. Sci Adv *2*, e1601625.
664 Hipp, M.S., Park, S.H., and Hartl, F.U. (2014). Proteostasis impairment in protein-misfolding and -
665 aggregation diseases. Trends Cell Biol *24*, 506-514.
666 Hoffmann, A., Becker, A.H., Zachmann-Brand, B., Deuerling, E., Bukau, B., and Kramer, G.
667 (2012). Concerted action of the ribosome and the associated chaperone trigger factor
668 confines nascent polypeptide folding. Mol Cell *48*, 63-74.

669 Hoffmann, A., Bukau, B., and Kramer, G. (2010). Structure and function of the molecular
670 chaperone Trigger Factor. Biochim Biophys Acta *1803*, 650-661.
671 Huang, C., and Kalodimos, C.G. (2017). Structures of Large Protein Complexes Determined by
672 Nuclear Magnetic Resonance Spectroscopy. Annu Rev Biophys *46*, 317-336.
673 Huang, C., Rossi, P., Saio, T., and Kalodimos, C.G. (2016). Structural basis for the antifolding
674 activity of a molecular chaperone. Nature *537*, 202-206.
675 Kaiser, C.M., Chang, H.-C., Agashe, V.R., Lakshmipathy, S.K., Etchells, S.A., Hayer-Hartl, M.,
676 Hartl, F.U., and Barral, J.M. (2006). Real-time observation of trigger factor function on
677 translating ribosomes. Nature *444*, 455-460.
678 Kampinga, H.H., and Craig, E.A. (2010). The HSP70 chaperone machinery: J proteins as drivers
679 of functional specificity. Nat Rev Mol Cell Biol *11*, 579-592.
680 Koldewey, P., Stull, F., Horowitz, S., Martin, R., and Bardwell, J.C.A. (2016). Forces Driving
681 Chaperone Action. Cell *166*, 369-379.
682 Libich, D.S., Tugarinov, V., and Clore, G.M. (2015). Intrinsic unfoldase/foldase activity of the
683 chaperonin GroEL directly demonstrated using multinuclear relaxation-based NMR. Proc Natl
684 Acad Sci U S A *112*, 8817-8823.
685 Maier, R., Eckert, B., Scholz, C., Lilie, H., and Schmid, F.X. (2003). Interaction of trigger factor
686 with the ribosome. J Mol Biol *326*, 585-592.
687 Mainz, A., Peschek, J., Stavropoulou, M., Back, K.C., Bardiaux, B., Asami, S., Prade, E., Peters,
688 C., Weinkauf, S., Buchner, J.*, et al.* (2015). The chaperone alphaB-crystallin uses different
689 interfaces to capture an amorphous and an amyloid client. Nat Struct Mol Biol *22*, 898-905.
690 Martinez-Hackert, E., and Hendrickson, W.A. (2007). Structures of and interactions between
691 domains of trigger factor from Thermotoga maritima. Acta Crystallogr D Biol Crystallogr *63*, 536-
692 547.
693 Martinez-Hackert, E., and Hendrickson, W.A. (2009). Promiscuous substrate recognition in
694 folding and assembly activities of the trigger factor chaperone. Cell *138*, 923-934.
695 Mattoo, R.U., and Goloubinoff, P. (2014). Molecular chaperones are nanomachines that
696 catalytically unfold misfolded and alternatively folded proteins. Cell Mol Life Sci *71*, 3311-3325.
697 Mayer, M.P., and Bukau, B. (2005). Hsp70 chaperones: cellular functions and molecular
698 mechanism. Cell Mol Life Sci *62*, 670-684.
699 Merz, F., Hoffmann, A., Rutkowska, A., Zachmann-Brand, B., Bukau, B., and Deuerling, E.
700 (2006). The C-terminal domain of Escherichia coli trigger factor represents the central module
701 of its chaperone activity. J Biol Chem *281*, 31963-31971.
702 Morgado, L., Burmann, B.M., Sharpe, T., Mazur, A., and Hiller, S. (2017). The dynamic dimer
703 structure of the chaperone Trigger Factor. Nat Commun *8*, 1992.
704 O'Brien, E.P., Christodoulou, J., Vendruscolo, M., and Dobson, C.M. (2012). Trigger Factor
705 Slows Co-translational Folding through Kinetic Trapping while Sterically Protecting the Nascent
706 Chain from Aberrant Cytosolic Interactions. J Am Chem Soc *134*, 10920-10932.
707 Oh, E., Becker, A.H., Sandikci, A., Huber, D., Chaba, R., Gloge, F., Nichols, R.J., Typas, A.,
708 Gross, C.A., Kramer, G.*, et al.* (2011). Selective ribosome profiling reveals the cotranslational
709 chaperone action of trigger factor in vivo. Cell *147*, 1295-1308.
710 Patzelt, H., Kramer, G., Rauch, T., Schönfeld, H.-J., Bukau, B., and Deuerling, E. (2002).
711 Three-state equilibrium of Escherichia coli trigger factor. Biol Chem *383*, 1611-1619.
712 Powers, E.T., and Balch, W.E. (2013). Diversity in the origins of proteostasis networks--a driver
713 for protein function in evolution. Nat Rev Mol Cell Biol *14*, 237-248.
714 Ries, F., Carius, Y., Rohr, M., Gries, K., Keller, S., Lancaster, C.R.D., and Willmund, F. (2017).
715 Structural and molecular comparison of bacterial and eukaryotic trigger factors. Sci Rep *7*, 10680.
716 Rosenzweig, R., Sekhar, A., Nagesh, J., and Kay, L.E. (2017). Promiscuous binding by Hsp70
717 results in conformational heterogeneity and fuzzy chaperone-substrate ensembles. Elife *6*.

718 Rossi, P., Xia, Y., Khanra, N., Veglia, G., and Kalodimos, C.G. (2016). (15)N and (13)C-
719 SOFAST-HMQC editing enhances 3D-NOESY sensitivity in highly deuterated, selectively
720 [(1)H,(13)C]-labeled proteins. J Biomol NMR *66*, 259-271.
721 Rutkowska, A., Mayer, M.P., Hoffmann, A., Merz, F., Zachmann-Brand, B., Schaffitzel, C., Ban,
722 N., Deuerling, E., and Bukau, B. (2008). Dynamics of trigger factor interaction with translating
723 ribosomes. J Biol Chem *283*, 4124-4132.
724 Saibil, H.R., Fenton, W.A., Clare, D.K., and Horwich, A.L. (2013). Structure and allostery of the
725 chaperonin GroEL. J Mol Biol *425*, 1476-1487.
726 Saio, T., Guan, X., Rossi, P., Economou, A., and Kalodimos, C.G. (2014). Structural basis for
727 protein antiaggregation activity of the trigger factor chaperone. Science *344*, 1250494.
728 Sekhar, A., Rosenzweig, R., Bouvignies, G., and Kay, L.E. (2016). Hsp70 biases the folding
729 pathways of client proteins. Proc Natl Acad Sci U S A *113*, E2794-2801.
730 Shen, Y., Delaglio, F., Cornilescu, G., and Bax, A. (2009). TALOS+: a hybrid method for
731 predicting protein backbone torsion angles from NMR chemical shifts. J Biomol NMR *44*, 213-
732 223.
733 Stull, F., Koldewey, P., Humes, J.R., Radford, S.E., and Bardwell, J.C.A. (2016). Substrate
734 protein folds while it is bound to the ATP-independent chaperone Spy. Nat Struct Mol Biol *23*, 53-
735 58.
736 Taylor, J.D., Hawthorne, W.J., Lo, J., Dear, A., Jain, N., Meisl, G., Andreasen, M., Fletcher, C.,
737 Koch, M., Darvill, N.*, et al.* (2016). Electrostatically-guided inhibition of Curli amyloid nucleation by
738 the CsgC-like family of chaperones. Sci Rep *6*, 24656.
739 Tzeng, S.R., Pai, M.T., and Kalodimos, C.G. (2012). NMR studies of large protein systems.
740 Methods Mol Biol *831*, 133-140.
741 Ullers, R.S., Ang, D., Schwager, F., Georgopoulos, C., and Genevaux, P. (2007). Trigger
742 Factor can antagonize both SecB and DnaK/DnaJ chaperone functions in Escherichia coli. Proc
743 Natl Acad Sci USA *104*, 3101-3106.
744 Uthailak, N., Mahamad, P., Chittavanich, P., Yanarojana, S., Wijagkanalan, W., Petre, J., and
745 Panbangred, W. (2017). Molecular Cloning, Structural Modeling and the Production of Soluble
746 Triple-Mutated Diphtheria Toxoid (K51E/G52E/E148K) Co-expressed with Molecular Chaperones
747 in Recombinant Escherichia coli. Mol Biotechnol *59*, 117-127.
748 Verba, K.A., Wang, R.Y., Arakawa, A., Liu, Y., Shirouzu, M., Yokoyama, S., and Agard, D.A.
749 (2016). Atomic structure of Hsp90-Cdc37-Cdk4 reveals that Hsp90 traps and stabilizes an
750 unfolded kinase. Science *352*, 1542-1547.
751 Walti, M.A., Schmidt, T., Murray, D.T., Wang, H., Hinshaw, J.E., and Clore, G.M. (2017).
752 Chaperonin GroEL accelerates protofibril formation and decorates fibrils of the Het-s prion
753 protein. Proc Natl Acad Sci U S A *114*, 9104-9109.
754 Wruck, F., Avellaneda, M.J., Koers, E.J., Minde, D.P., Mayer, M.P., Kramer, G., Mashaghi, A.,
755 and Tans, S.J. (2017). Protein Folding Mediated by Trigger Factor and Hsp70: New Insights from
756 Single-Molecule Approaches. J Mol Biol.
757 Zhuravleva, A., Clerico, E.M., and Gierasch, L.M. (2012). An interdomain energetic tug-of-war
758 creates the allosterically active state in Hsp70 molecular chaperones. Cell *151*, 1296-1307.
759

Supporting Information

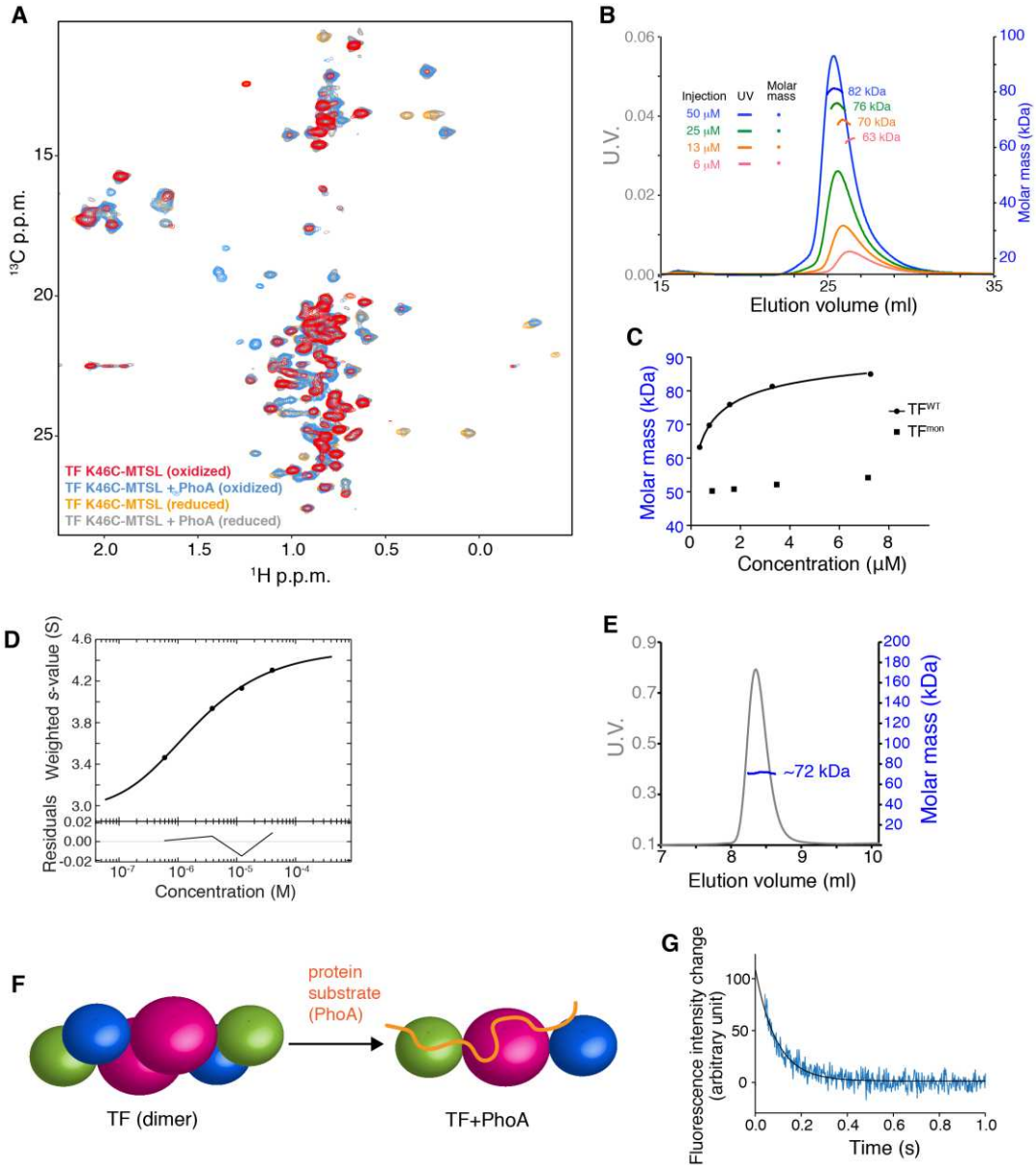

Figure 1-figure supplement 1. Dynamic monomer-dimer transition of TF.

(*A*) Observation of PRE for TF K46C attached with MTSL in the presence and absence of its substrate PhoA. Overlay of ^{1}H-^{13}C methyl HMQC spectra of [U-^{2}H; Met-$^{13}CH_3$; Ile-δ1-$^{13}CH_3$; Leu,Val-$^{13}CH_3$/$^{13}CH_3$]-labeled TF K46C attached with MTSL in oxidized (paramagnetic) and reduced (diamagnetic) conditions. Reduced spectra were acquired in the presence of ascorbic acid. A number of resonances of unliganded TF broadened

768 out in paramagnetic spectrum indicate strong intermolecular PRE due to dimer
769 formation. Addition of unfolded substrate protein PhoA retrieved the broadened
770 resonances, indicating the dissociation of the dimer by the interaction with the
771 substrate. (*B*) SEC-MALS of TF injected at varying concentrations. Injection at lower
772 concentration resulted lower molecular mass, indicating increase of monomer fraction
773 at lower concentration. (*C*) Plots of molar mass as a function of concentration. The
774 molar mass was estimated by SEC-MALS for TF and TF^{mon} (TF V39E/I76E/I80A)
775 injected at varying concentrations. The solid line represents the fit of the data to a
776 model of monomer-dimer equilibrium. (*D*) Sedimentation velocity-AUC isotherm of TF.
777 Best-fit isotherms of the weight-average s-values, sw(c), obtained by integration of c(s)
778 distributions of TF over the entire s-range for each loading concentration in a dilution
779 series. The solid line is the fitted isotherm to a reversible monomer-dimer self-
780 association model. The dissociation constant K_d is 1.687 [1.482, 1.914] μM. Errors of the
781 constants represent the 68.3% confidence interval (CI) using an automated surface
782 projection method. (*E*) SEC-MALS of TF in complex with PhoA1-141 shows that TF
783 binds to PhoA as a monomer (TF-PhoA theoretical molar mass: 66 kDa). (*F*) Schematic
784 showing the monomerization of TF upon substrate-binding. (*G*) Dissociation kinetics of
785 the TF dimer. Dissociation of the dimer was initiated by 10-fold dilution of TF to final
786 concentration of 0.1 μM at 22 °C. Solid line represents the fit of the data to a single
787 exponential function yielding the dissociation rate (k_{diss}) of ~10 s^{-1}.
788

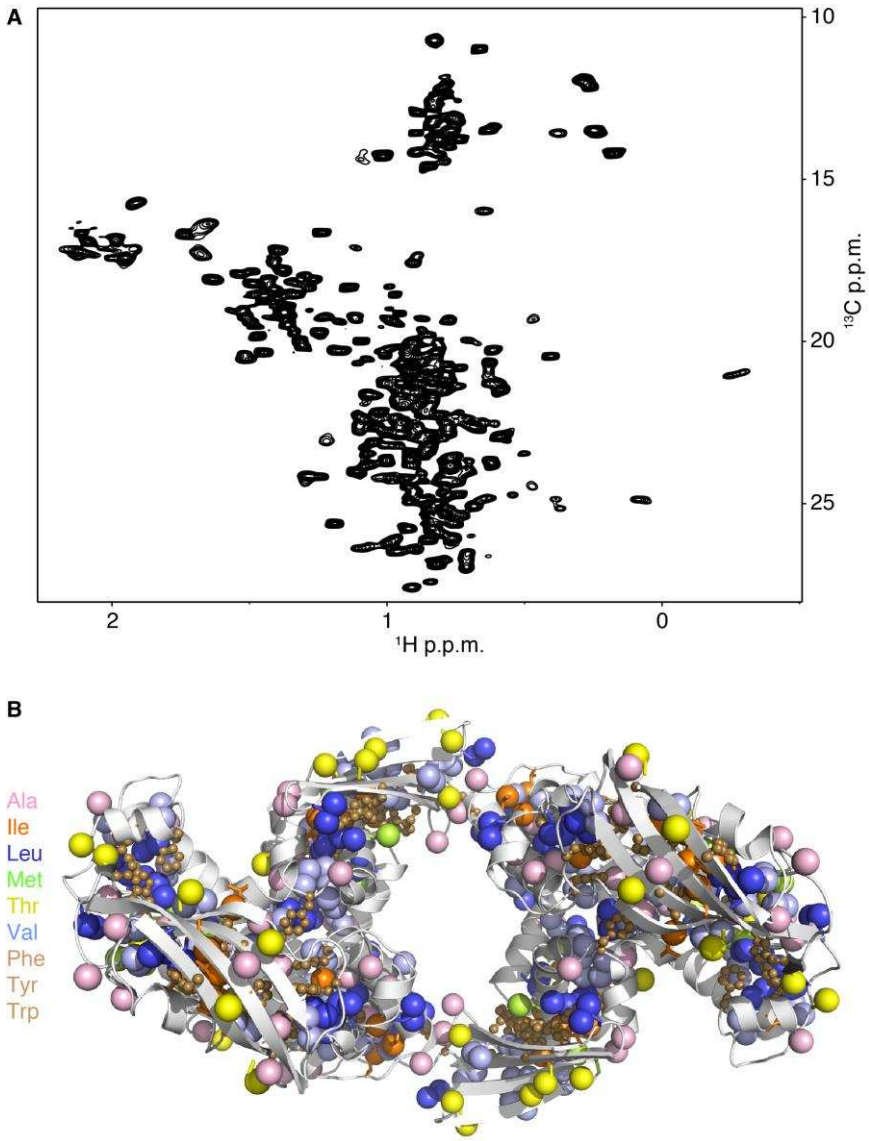

789

790 Figure 2-figure supplement 1. NMR of dimeric TF.

791 (*A*) ^{1}H–^{13}C methyl HMQC spectrum of [U-^{2}H; Ala-$^{13}CH_3$; Met-$^{13}CH_3$; Ile-δ1-$^{13}CH_3$;

792 Leu,Val-$^{13}CH_3$/$^{13}CH_3$; Thr-$^{13}CH_3$]-labelled TF. (*B*) TF is enriched in hydrophobic amino

793 acids, such as methyl-bearing (Ala, Ile, Leu, Met, Thr and Val) and aromatic (Phe, Tyr

794 and Trp).

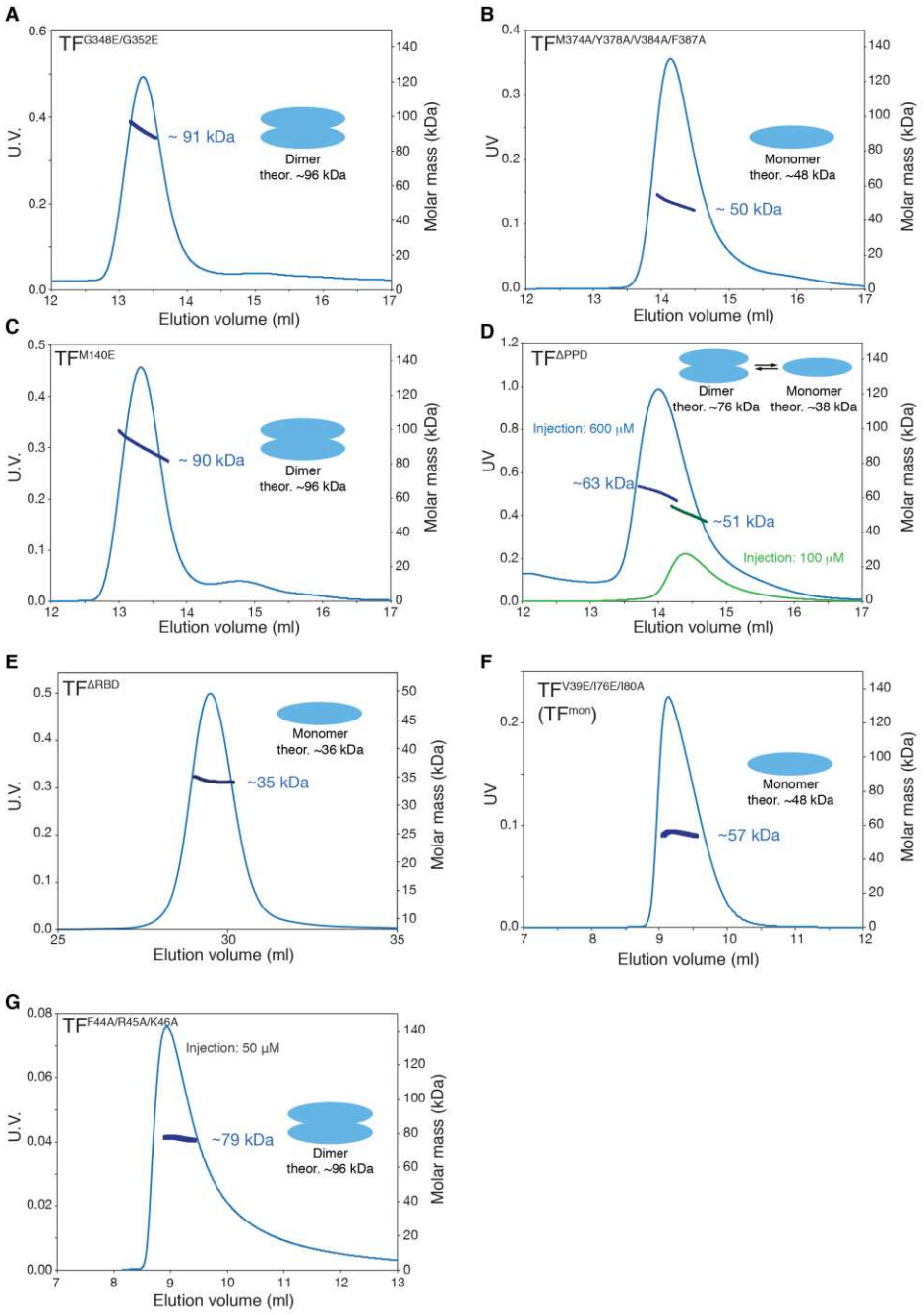

795

796 Figure 2-figure supplement 2. SEC-MALS of TF mutants.

797 SEC-MALS profiles of $TF^{G348E/G352E}$ (*A*), $TF^{M374A/Y378A/V384A/F387A}$ (*B*), TF^{M140E} (*C*), $TF^{\Delta PPD}$

798 (*D*), $TF^{\Delta RBD}$ (*E*), $TF^{V39E/I76E/I80A}$ (TF^{mon}) (*F*), and $TF^{F44A/R45A/K46A}$ (*G*) are shown. Proteins

799 were injected at the concentration of 100 μM unless otherwise stated. $TF^{G348E/G352E}$,

800 $TF^{M374A/Y378A/V384A/F387A}$, and TF^{M140E} have mutations on the substrate-binding site A, B,
801 and D, respectively. $TF^{F44A/R45A/K46A}$ has mutation at the ribosome-binding loop
802 containing the signature motif. Destabilization of the dimer by the introduction of
803 mutations on the substrate-binding site B as well as by deletion of PPD containing site E
804 supports the engagement of these substrate-binding sites in the dimerization (Figure
805 3B). Moderate effect of the deletion of PPD to dimerization implies that the contribution
806 of the interaction between PPD and RBD in the formation of the dimer is less significant
807 and is auxiliary. The mutations in the signature motif have little effect to the dimer
808 formation, which is consistent with the fact that only a part of the ribosome-binding
809 loop is involved in the dimer formation and the rest is floating in the cavity formed by
810 PPD and SBD (Figure 3-figure supplement 1A and B).
811

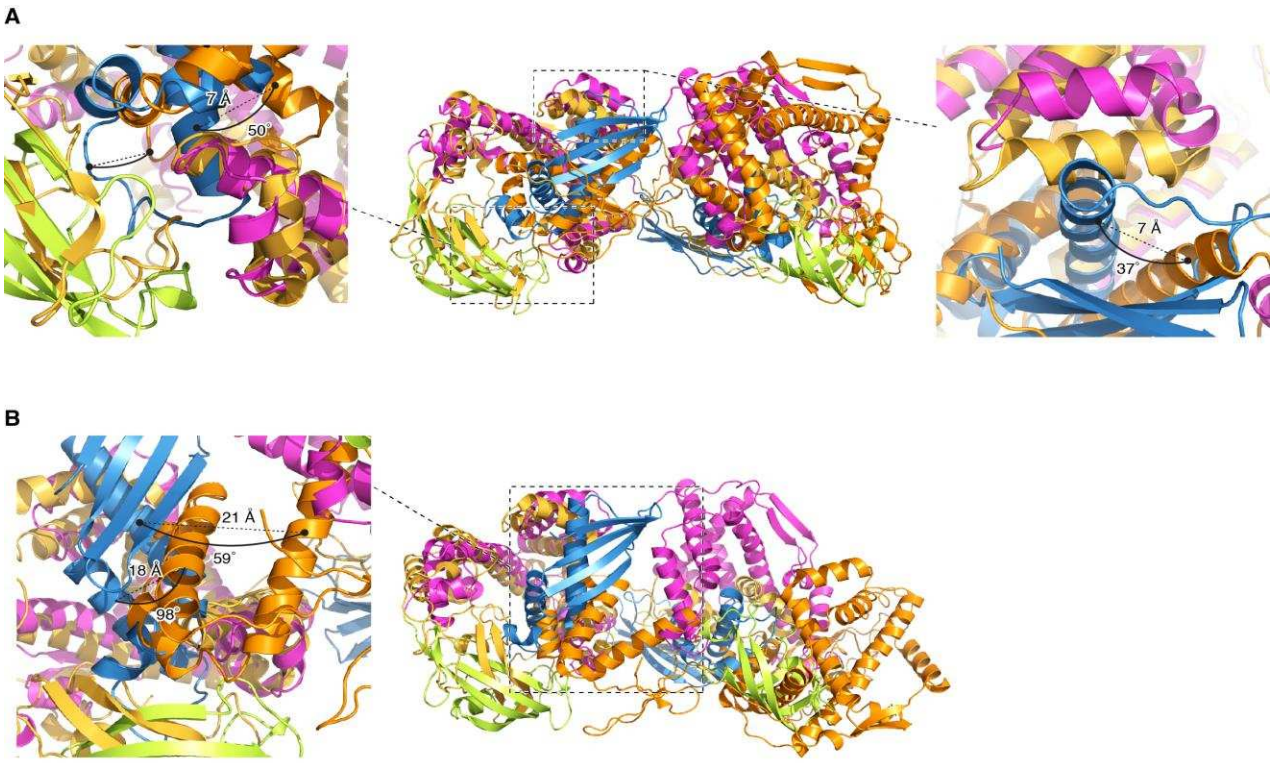

812

813 Figure 2-figure supplement 3. Comparison with PRE-based docking models.

814 The structure of TF dimer superimposed with previously reported PRE-based docking
815 models (Morgado et al., 2017); conformer 1 [PDB code: 5OWI] (*A*), and conformer 2 [PDB
816 code: 5OWJ] (*B*). PPD, SBD, and RBD in the structure of TF dimer are shown in green,
817 pink, and blue, respectively. The docking model is shown in orange and gold. The
818 coordinates are superimposed on the backbone heavy atoms of SBD. Differences in
819 rotation and translation of the helices in RBD between the previously reported PRE-
820 based docking model and the current dimer structure are indicated. Most of the
821 contacts, which are seen in the current structure of the TF dimer and were validated by
822 mutagenesis and chemical shift perturbation mapping, are not present in the PRE-based
823 models. In the PRE-derived conformer 1, RBD makes contacts with the arm 1 and the

PPD of the other subunit, which were also seen in the current dimer TF structure. However, in the PRE-derived conformer 1 the RBD makes no significant contacts with the arm 2, which is not consistent with the significant effect that mutations in the arm 2 have on the dimerization as shown by SEC-MALS (Figure 2-figure supplement 2B). The PRE-derived conformer 2 has RBD snagged on the tips of the arm 1 and arm 2, as well as on the edge of PPD. A very small overlap between the substrate-binding sites and the dimer interface is seen in the PRE-derived conformer 2. In contrast, in the current structure of TF dimer, RBD is buried inside the cradle formed by SBD and PPD of the other subunit, thus explaining why the TF dimer dissociates upon binding to the substrate protein (Figure 1-figure supplement 1A, E, and F). In addition to the significant differences in the overall domain orientation between the PRE-derived models and the current TF structure, the RBD structure itself appears to be loosely packed in the PRE-derived models.

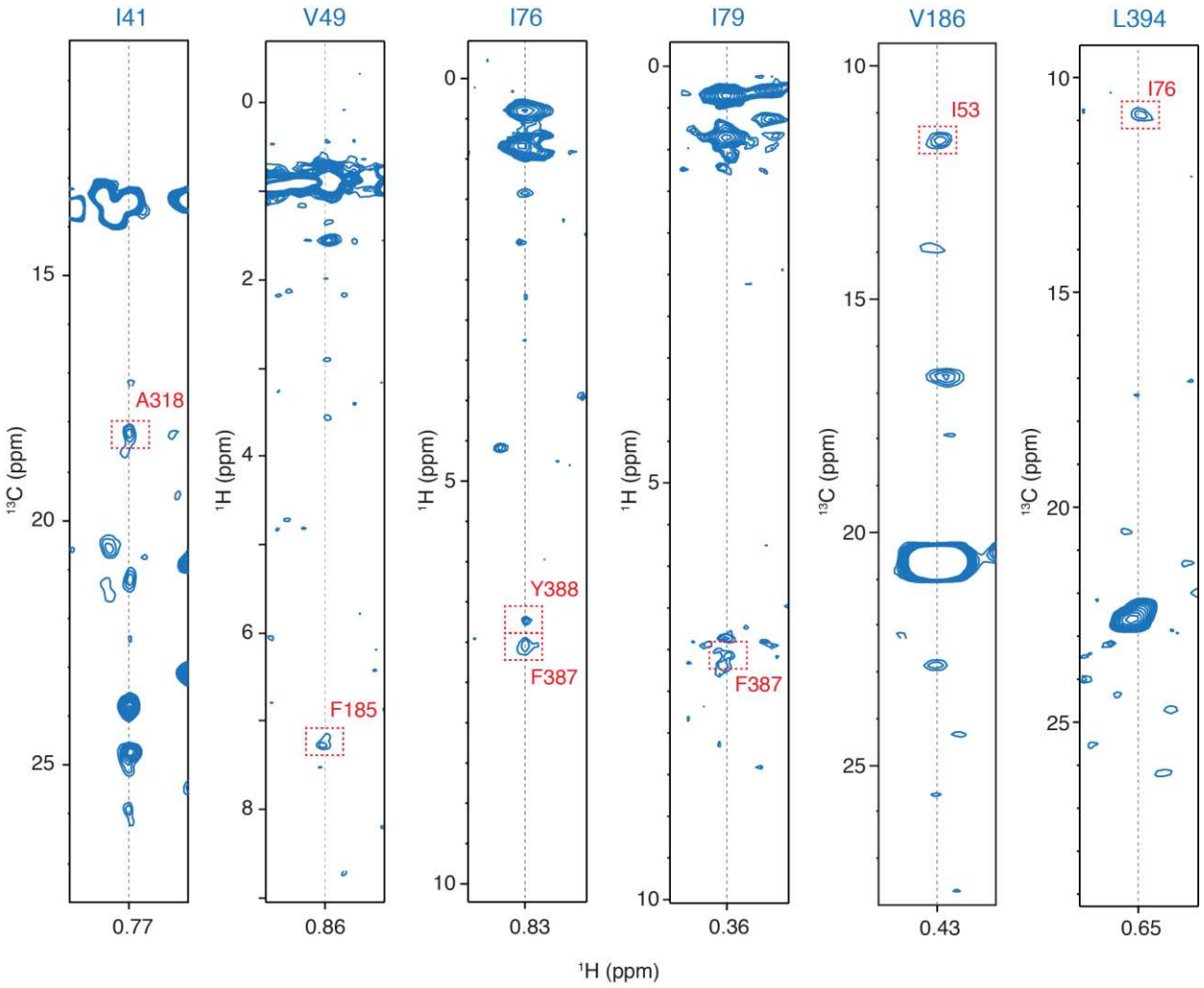

839

840

841 Figure 2-figure supplement 4. Examples of the inter-molecular NOEs.

842 Representative strips from ^{13}C-edited NOESY-HMQC and HMQC-NOESY-HMQC NMR

843 experiments. The intermolecular NOE cross peaks are designated by a dashed-line red

844 rectangle.

845

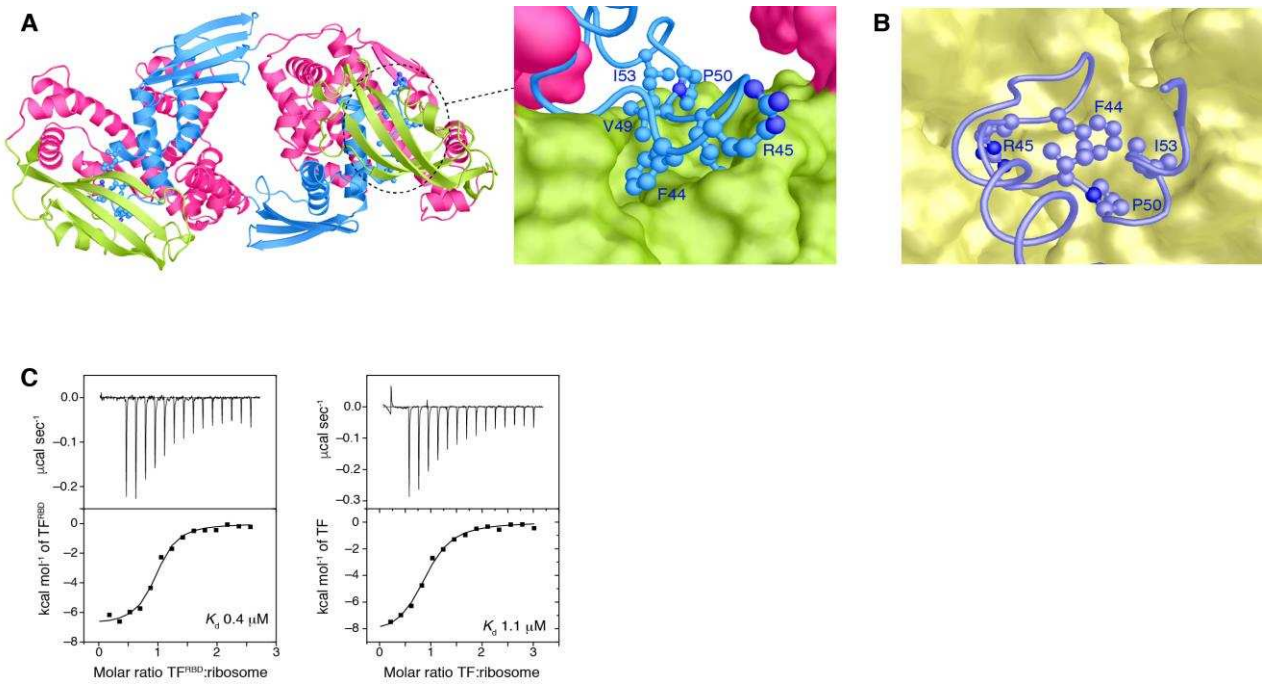

846

847

848 Figure 3-figure supplement 1**.** The ribosome-binding loop in the TF dimer.

849 Close-up view of the ribosome-binding loop in the TF dimer (*A*) or TF in complex with

850 the ribosome (PDB ID: 1W2B) (*B*). The amino acid residues of the ribosome-binding

851 loop involved in the interaction are shown in ball-and-stick. PPD, SBD, and RBD are

852 shown in green, pink, and blue, respectively. The ribosome is represented as yellow

853 surface model. (*C*) ITC traces of the titration of TF (right) and RBD (left) to the

854 ribosome. Titration of RBD indicated slightly stronger affinity than that of TF, which is

855 consistent with the fact that RBD is responsible for the binding to the ribosome and the

856 ribosome-binding loop is protected in the TF dimer. The experiments were performed

857 at 22 °C.

858

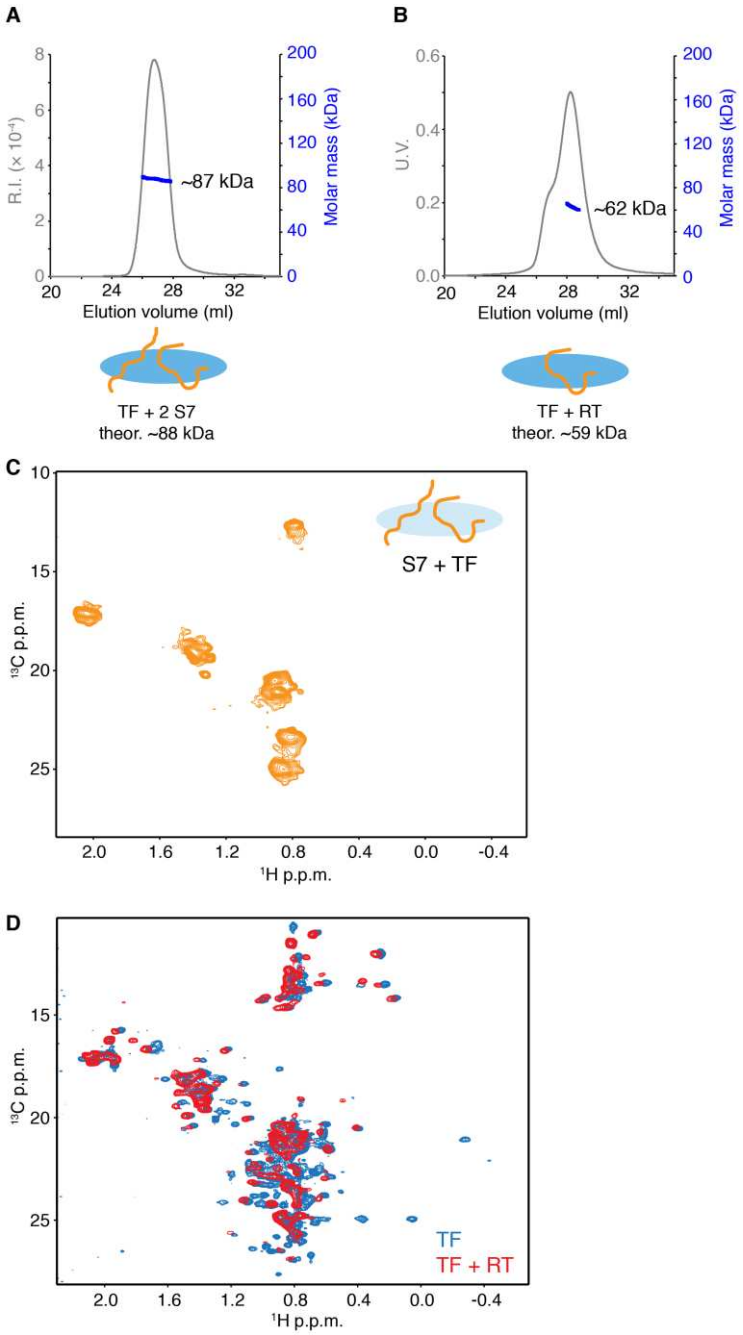

859

860 Figure 3-figure supplement 2. Characterization of small substrate proteins in complex

861 with TF.

862 (*A*) SEC-MALS of *E. coli* S7 in complex with TF indicating two S7 molecules bind to the

863 monomer of TF. (*B*) SEC-MALS of *E. coli* reverse transcriptase (RT)-Ec86 255-320 in

complex with TF indicating one RT molecule binds to the monomer of TF. Unliganded dimeric TF eluted before TF-RT complex, resulting in a shoulder on the left side of the main peak. (*C*) ^{1}H-^{13}C methyl HMQC of [U-^{2}H; Met-$^{13}CH_3$; Ala-$^{13}CH_3$; Ile-δ1-$^{13}CH_3$; Leu,Val-$^{13}CH_3$/$^{13}CH_3$]-labeled S7 in complex with unlabeled TF showing narrow dispersion of the resonances of methyl groups in S7. (*D*) Overlay of ^{1}H-^{13}C methyl HMQC of [U-^{2}H; Met-$^{13}CH_3$; Ala-$^{13}CH_3$; Ile-δ1-$^{13}CH_3$; Leu,Val-$^{13}CH_3$/$^{13}CH_3$]-labeled TF (blue) and TF-RT complex (red). Several resonances that broaden out in complex with RT are located at the substrate-binding sites on TF. Most of the dispersed resonances observed in the spectrum of TF-RT complex match to the resonances of TF and no dispersed resonances are found for RT, which suggests that RT in complex with TF does not form a folded structure. The results indicate that both of RT and S7 binds to monomeric TF as an unfolded state, although the possibility of the existence of minor folded population cannot be excluded.

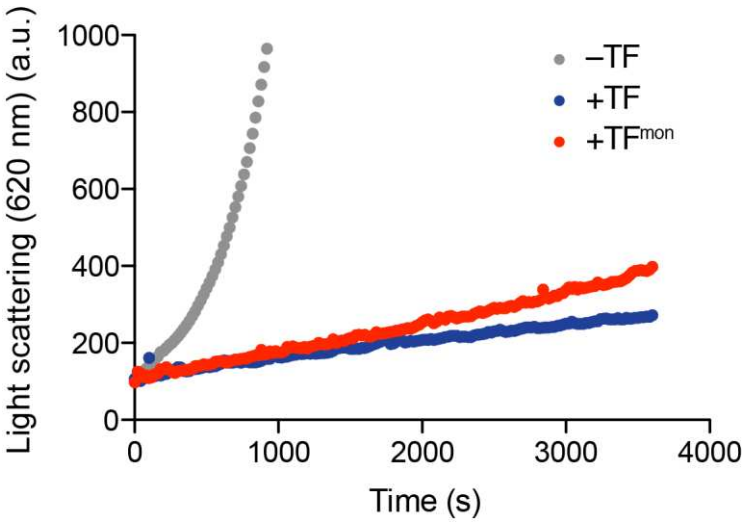

Figure 4-figure supplement 1. Aggregation of GAPDH in the absence or presence of 1 μM TF and TF^{mon}. The aggregation of GAPDH was monitored by 90° light scattering at 620 nm.

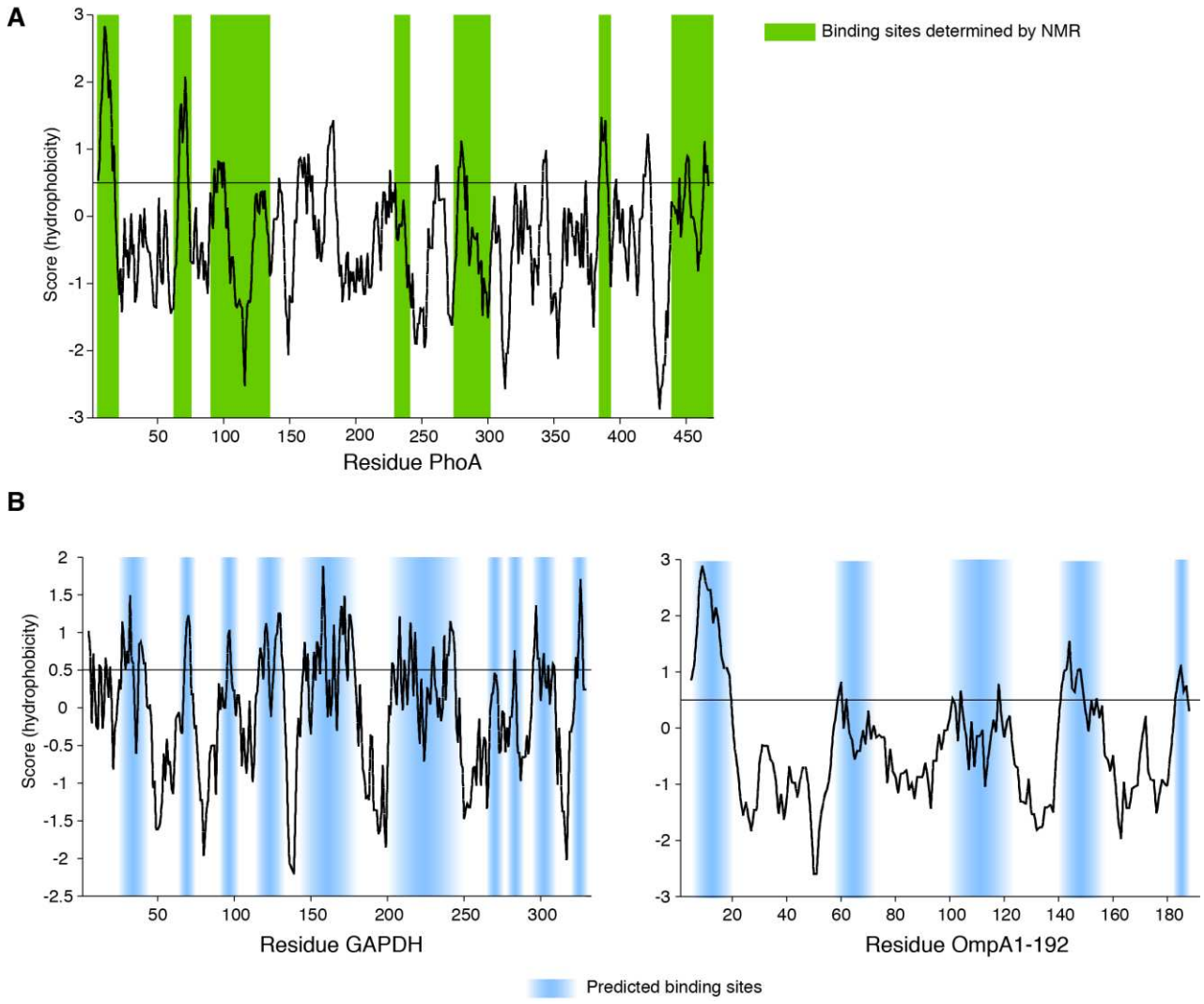

Figure 4-figure supplement 2. Sequence hydrophobicity of the substrate proteins of TF (Roseman algorithm, window = 9). (A) Hydrophobicity plot of PhoA as a function of its primary sequence. TF-binding sites determined by NMR (Saio et al., 2014) are highlighted in green. (B) Hydrophobicity plot of GAPDH (left panel) and $OmpA^{1-192}$ (right panel) as a function of their primary sequences. The hydrophobic stretches that are expected to bind to TF are highlighted in light blue.

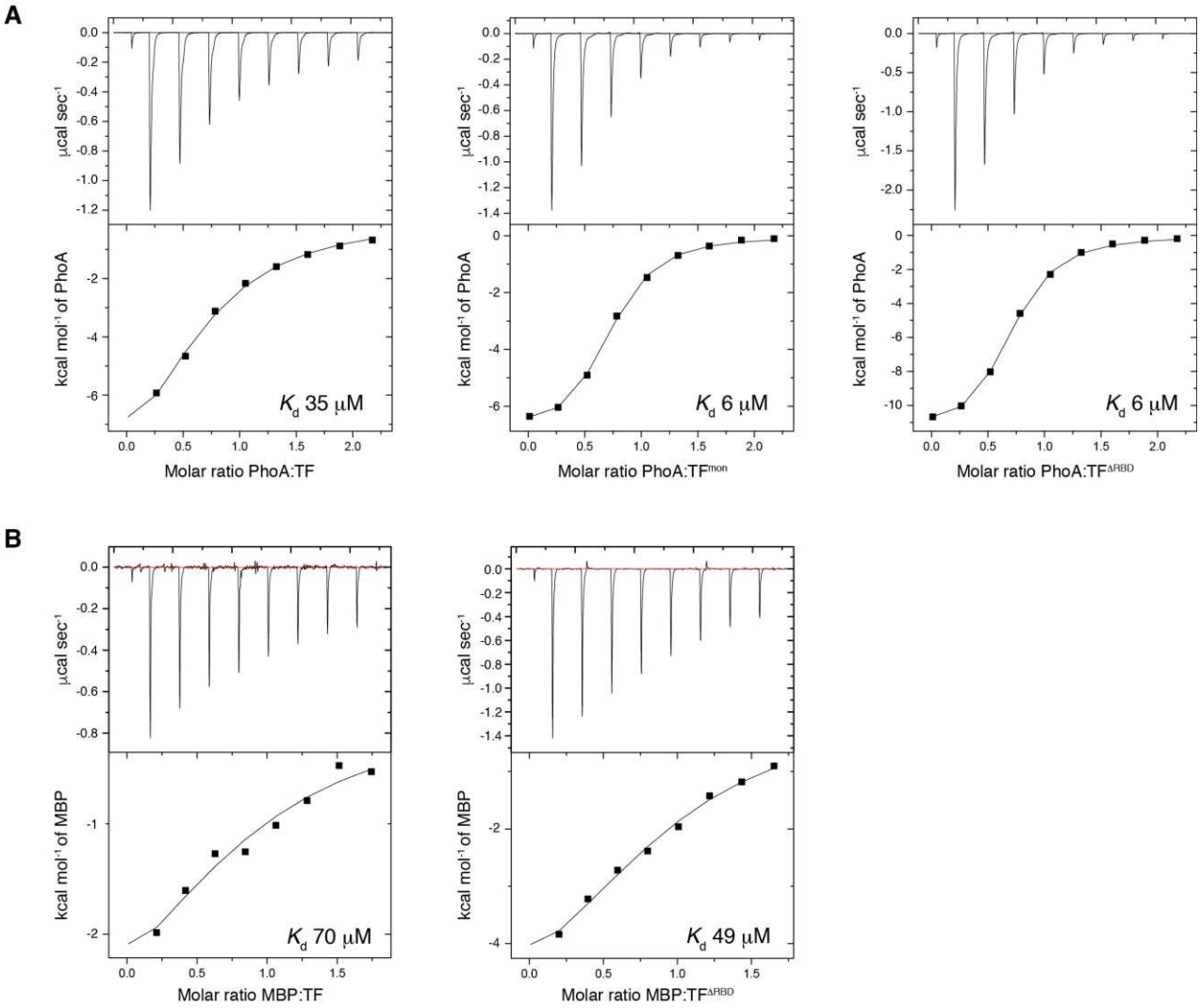

896

897 Figure 5-figure supplement 1. ITC traces of the titration of unfolded proteins to TF.

898 ITC traces of the titration of PhoA220-310 (*A*) into TF (left panel), TF^{mon} (middle

899 panel), and TF$^{\Delta RBD}$ (right panel), or MBP198-265 (*B*) into TF (left panel) and TF$^{\Delta RBD}$

900 (right panel), Monomeric variants of TF indicated stronger affinity to the unfolded

901 substrates, which is consistent with the fact that the three of the substrate-binding sites

902 are buried in the dimer. The titration of PhoA220-310 and MBP198-265 were

903 performed at 8 and 22 °C, respectively.

904

A

	Accessible surface area [Å] Monomer	Dimer	Ratio (Dimer/Monomer)
Site A	314	254	0.81
Site B	757	469	0.62
Site C	550	222	0.40
Site D	358	293	0.82
Site E	571	430	0.75
Total	2552	1669	0.65

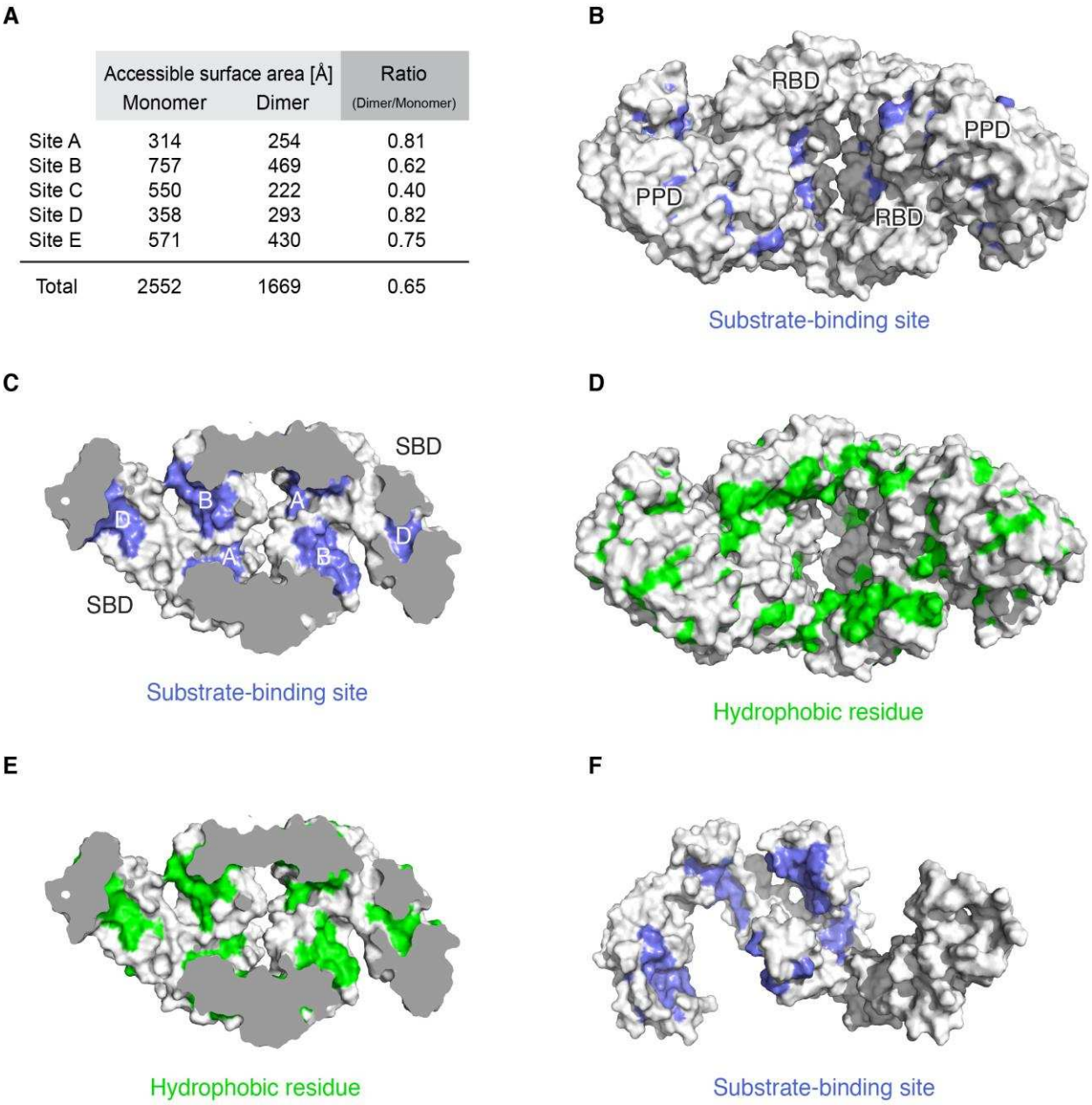

905

906 Figure 5-figure supplement 2. Substrate-binding sites in the dimer.

907 (*A*) Accessible surface area of the substrate-binding sites in monomeric and dimeric

908 TF. (*B*) The residues identified by NMR to interact with unfolded MBP are colored blue

909 on the surface of TF dimer. (*C*) Cut-away view of the TF dimer with the mapping of

910 substrate-binding sites as in the panel B. Substrate-binding sites A, B and D are

assembled on the inner surface of the cavity in the dimer, forming a single broad substrate-binding site. (*D*) Mapping of hydrophobic residues colored green on the surface of TF dimer. The pore of the dimer is paved with a large hydrophobic surface on RBD that leads into the cavity. (*E*) Cut-away view of the TF dimer with the mapping of hydrophobic residues as in the panel D. (*F*) The mapping of the substrate-binding sites colored blue on the surface of the crystal structure of monomeric TF [PDB code: 1W26].

918